N O T I C E

THIS DOCUMENT HAS BEEN REPRODUCED FROM MICROFICHE. ALTHOUGH IT IS RECOGNIZED THAT CERTAIN PORTIONS ARE ILLEGIBLE, IT IS BEING RELEASED IN THE INTEREST OF MAKING AVAILABLE AS MUCH INFORMATION AS POSSIBLE

Numerical Investigation of Turbulent Channel Flow

Parviz Moin and John Kim

July 1981

NASA

Numerical Investigation of Turbulent Channel Flow

Parviz Moin
John Kim, Stanford University, Stanford, California and
Ames Research Center, Moffett Field, California

NUMERICAL INVESTIGATION OF TURBULENT CHANNEL FLOW

Parvis Moin[*] and John Kim[*]
Department of Mechanical Engineering
Stanford University, Stanford, CA 94305

Fully developed turbulent channel flow has been simulated numerically at Reynolds number 13800, based on centerline velocity and channel half width. The large-scale flow field has been obtained by directly integrating the filtered, three-dimensional, time-dependent, Navier-Stokes equations. The small-scale field motions were simulated through an eddy viscosity model. The calculations were carried out on the ILLIAC IV computer with up to 516,096 grid points.

The computed flow field was used to study the statistical properties of the flow as well as its time-dependent features. The agreement of the computed mean velocity profile, turbulence statistics, and detailed flow structures with experimental data is good. The resolvable portion of the statistical correlations appearing in the Reynolds stress equations are calculated. Particular attention is given to the examination of the flow structure in the vicinity of the wall.

1. Introduction

Large-eddy simulation (LES) is a relatively new approach to the calculation of turbulent flows. The basic idea stems from two experimental observations. First, the large-scale structure of turbulent flows varies greatly from flow to flow (e.g., jets vs. boundary layers) and consequently is difficult, if not impossible, to model in a general way. Second, the small-scale turbulence structures are nearly isotropic, very universal in character (Chapman, 1979) and hence much more amenable to general modeling. In LES, one actually calculates the large-scale motions in a time-dependent, three-

---

dimensional computation, using for the large-scale field dynamical equations that incorporate simple models for small-scale turbulence. Only the part of the turbulence field with scales that are small relative to overall dimensions of the flow field is modeled. This is in contrast to phenomenological turbulence modeling, in which all the deviations from the mean velocity profile are modeled.

A typical LES calculation for wall-bounded turbulent flows imposes a great demand on computer speed and memory. At present, therefore, the use of LES for practical engineering applications is admittedly uneconomical. However, for simple flows, such calculations are just within reach of the largest present computers. The information generated by these computations can in turn be used as a powerful research tool in studies of the structure and dynamics of turbulence. In addition, the various correlations that can be obtained from the computed large-scale flow field may be used in developing phenomenological turbulence models for complex flows. These are the considerations that motivate the present development of the LES method.

The first application of LES was made by Deardorff (1970), who simulated a turbulent channel flow at an indefinitely large Reynolds number. In this pioneering work he showed that three-dimensional computation of turbulence (at least for simple flows) is feasible. Using only 6,720 grid points, he was able to predict several features of turbulent channel flow with a fair amount of success. Of particular significance was the demonstration of the potential of LES for use in basic studies of turbulence.

Following Deardorff's work, Schumann (1973, 1975) also calculated turbulent channel flow and extended the method to cylindrical geometries (annuli). He used up to ten times more grid points (65,536) than Deardorff and an improved subgrid scale (SGS) model. In addition to dividing SGS stresses into

2

a locally isotropic part and an inhomogeneous part, he employed a separate partial differential equation for SGS turbulent kinetic energy. However, the added differential equation did not improve the results over the calculations in which only an eddy viscosity model was used (Schumann, 1975).

Grötzbach and Schumann (1977) extended their channel flow calculations to account for temperature fluctuations and heat transfer. Later extensions by Grötzbach include calculations of secondary flows in partly roughened channels, inclusion of buoyancy effects, and liquid metal flows in plane channels and annuli. A recent review of this group's work in LES was given by Schumann et al. (1979).

In all of the above computations, the dynamics of the inner region of the boundary layer (viscous sublayer and buffer layer) was essentially ignored. It is in this region that virtually all of the production of turbulence kinetic energy takes place (Townsend, 1956; Kim et al., 1971). Artificial boundary conditions in the logarithmic region were used to simulate the inner layers. Aside from the fact that these boundary conditions are designed to be consistent in the mean with the law of the wall, there is little justification or experimental evidence to warrant their use for the detailed flow field. However, the computations of Deardorff (1970) and especially those of the Karlsruhe group have produced successful comparisons with experimental data in the regions away from the walls. With a relatively modest number of grid points, they have been able to extract considerable information of practical interest from their computations.

The first numerical simulation of turbulent channel flow that computed rather than modeled the flow in the immediate neighborhood of the wall was that of Moin et al. (1978). In this calculation only 16 uniformly spaced grid points were used in each of the streamwise, x, and spanwise, z, directions

3

and 65 non-uniformly spaced grid points in the direction normal to the walls. The computational grid resolution in the lateral directions was inadequate for resolving the experimentally observed coherent structures in the viscous sublayer. Nevertheless, the computations did display some of the well-established features of the flow in the wall region. The results of this computation were encouraging enough to justify the undertaking of the present calculations.

In this paper, we describe our numerical studies of incompressible turbulent channel flow with up to 516,096 grid points. Particular attention is given to the investigation of the detailed flow structures. The Reynolds number, Re_τ, based on shear velocity, u_τ, and channel half-width was set at 640. The corresponding Reynolds number based on centerline velocity and channel half-width is about 13800 (Hussain and Reynolds, 1975). The results of this work can be summarized briefly by stating that, in the present computations, the calculated mean velocity profile and turbulence statistics are in good agreement with the experimental data. The detailed time-dependent flow structures are strikingly similar to those observed experimentally. In addition, the resolvable portion of several statistical correlations which play an important role in phenomenological turbulence modeling are computed. These results tend to indicate that the LES method can be used very effectively in supplementing laboratory measurements of turbulent shear flows.

2. Governing Equations for the Large-Scale Field

In LES, each flow variable f is decomposed as follows:

$$f = \bar{f} + f' \tag{2.1}$$

where $\bar{f}$ is the large-scale component and f' is the residual field.

Following Leonard (1974), we define the large-scale field as

$$\overline{f}(x_1,x_2,x_3) = \int_D \prod_{i=1}^{3} G_i(x_i,x_i') \; f(x_1',x_2',x_3') \; dx_1'dx_2'dx_3' \qquad (2.2)$$

where G_i is the filter function in the i-direction and the integral is extended over the whole flow field. In planes parallel to the walls in which the flow is statistically homogeneous, we use the Gaussian filter function:

$$G_i(x_i,x_i') = \left(\frac{6}{\pi \Delta_i}\right)^{1/2} \exp\left[-6(x_i - x_i')^2/\Delta_i^2\right] , \qquad i = 1,3 \qquad (2.3)$$

Here, $\Delta_i = 2h_i$ (Kwak et al., 1975), h_i is the computational mesh size in the i-direction, and subscripts 1 and 3 refer to the streamwise and spanwise directions, respectively. The corresponding integrals in (2.2) are extended over the entire (x_1,x_3) plane. The width of the Gaussian function characterizes the size of the smallest eddies in the homogeneous directions that are retained in the filtered field (the largest eddies in the residual field).

Due to variation of turbulence length scale in the direction normal to the walls, x_2, one should use a filter with a variable width, $\Delta_2(x_2)$. In this direction a sectionally continuous "top hat" filter function was used. Let x_{2_j} be the location of the jth computational grid point in the vertical direction; we define the filter function G_2 for the control volume surrounding x_{2_j} as follows:

$$G_2(x_2,x_2') = \begin{cases} (\Delta^+(x_2) + \Delta^-(x_2))^{-1} & \text{for } x_2 - \Delta^-(x_2) < x_2' < x_2 + \Delta^+(x_2) \\ 0 & \text{for } x_2' > x_2 + \Delta^+(x_2) \text{ and } x_2' < x_2 - \Delta^-(x_2) \end{cases} \qquad (2.4)$$

where

$$\left.\begin{array}{l} \Delta^+(x_2) = \frac{1}{2}(x_{2_{j+1}} - x_{2_j}) \\[2mm] \Delta^-(x_2) = \frac{1}{2}(x_{2_j} - x_{2_{j-1}}) \end{array}\right\} \quad \text{for} \quad \frac{1}{2}(x_{2_j} + x_{2_{j-1}}) < x_2 < \frac{1}{2}(x_{2_{j+1}} + x_{2_j})$$

The functions Δ^+ and Δ^- are sectionally constant functions of x_2, therefore, in the open neighborhood surrounding each computational grid point, $x_{2_j} - \Delta^- < x_2 < x_{2_j} + \Delta^+$, $d\Delta^+/dx_2 = d\Delta^-/dx_2 = 0$. An important consequence of this property of Δ^+ and Δ^- and the form of G_1 and G_3 (function of $x_i - x_i'$, $i = 1,3$) is the commutivity of the filtering operation and partial differentiation operators in these neighborhoods and in particular at the computational grid points (see Moin et al. (1978)), i.e.,

$$\overline{\frac{\partial f}{\partial x_2}} = \frac{\partial \overline{f}}{\partial x_2} \tag{2.5}$$

Note that, with the application of G_2, the filtered variable $\overline{f}$ will be sectionally continuous and the filtering in (2.3) is interpreted as an average over grid spacings in the x_2-direction. This is a step prior to complete discretization of flow variables for numerical computation (Section 3).

Schumann (1975) and co-workers use a filtering function similar to (2.4) in all spatial directions. When applying this averaging process to the Navier-Stokes equations, they evaluate the integral in the direction of the derivatives analytically and then have to deal with averages over the faces of the control volumes. This process introduces three types of surface-averaged as well as volume-averaged variables. The extra variables have to be related to each other in some way.

Now, applying the filtering operation (2.2) to the incompressible Navier-Stokes and continuity equations, we obtain the dynamical equations of the large-scale flow field,

$$\frac{\partial \overline{u}_i}{\partial t} - \epsilon_{ijk}\overline{u}_j\overline{\omega}_k + \frac{\partial}{\partial x_i}\frac{1}{2}\overline{u}_j\overline{u}_j = -\frac{\partial P}{\partial x_i} + \delta_{i1} - \frac{\partial}{\partial x_j}\tau_{ij} + \frac{1}{Re_\tau}\frac{\partial^2 \overline{u}_i}{\partial x_j \partial x_j} \qquad (2.6)$$

$$\frac{\partial \overline{u}_i}{\partial x_i} = 0 \qquad (2.7)$$

where we have decomposed u_i as in (2.1) and

$$\omega_k = \epsilon_{pqk}\frac{\partial \overline{u}_q}{\partial x_p}$$

$$\tau_{ij} = Q_{ij} - \frac{Q_{kk}}{3}\delta_{ij} \qquad (2.8a)$$

$$Q_{ij} = \overline{u_i'u_j'} + \overline{u_j'\overline{u}_i} + \overline{\overline{u}_j u_i'} \qquad (2.8b)$$

$$P = \frac{\overline{P}}{\rho} + \frac{Q_{kk}}{3}$$

Here, the variables are non-dimensionalized using the channel half-width δ and the wall shear velocity u_τ. The calculations were carried out for a fixed streamwise mean-pressure gradient which is accounted for by the δ_{i1} term in the momentum equation (2.6).

There are two points associated with Eq. (2.6) that require further explanation. First, the convective term, $\frac{\partial}{\partial x_j}u_iu_j$, is written in the equivalent but more cumbersome form

$$- \epsilon_{ijk}u_j\omega_k + \frac{\partial}{\partial x_i}\frac{1}{2}u_ju_j$$

This was done because it can be shown (Mansour et al., 1977) that, with this form in the absence of time-differencing errors, conservation of energy, momentum, and circulation in inviscid flows will be obtained when virtually any difference scheme is applied to (2.6). Second, it should be noted that the so-called Leonard (1974) stress term

7

$$\lambda_{ij} = \overline{\overline{u_i}\,\overline{u_j}} - \overline{u_i}\,\overline{u_j} \qquad (2.9)$$

is _not_ equal to zero. One has the option of calculating the term with double bars explicitly, or, as Deardorff (1970) has done, to incorporate λ_{ij} in whatever modeling assumption is used for τ_{ij} (see the next section). In the present work, with respect to the Gaussian filter in the horizontal directions where the partial derivatives are calculated pseudospectrally (Sec. 5), we have chosen the former option. In Sec. 6 we shall show that λ_{ij} can be quite significant; hence, including it with τ_{ij} is not recommended. With respect to the top-hat filter in the x_2-direction where the derivatives are evaluated by second-order finite-difference schemes, the latter option was chosen. Here, it can be shown that (Shaanan et al., 1975) λ_{ij} is of the same form and order as the truncation error of the finite-difference scheme; hence its explicit calculation is not justified. However, when higher-order finite-difference schemes or spectral methods are used to evaluate the derivatives in the x_2-direction, λ_{ij} should be calculated explicitly.

3. Residual Stress Model

The basic idea behind large-eddy simulation is that the large-scale motions, which are calculated explicitly, provide most of the important turbulent transport and, hence, the influence of the small eddies can be modeled relatively crudely. In the present calculations, we have used an eddy viscosity model for τ_{ij} similar to that used by Schumann (1975).

$$\tau_{ij} = -2\nu_T(S_{ij} - \langle S_{ij} \rangle) - 2\nu_T^* \langle S_{ij} \rangle \qquad (3.1)$$

where

$$S_{ij} = \frac{1}{2}\left(\frac{\partial \overline{u}_i}{\partial x_j} + \frac{\partial \overline{u}_j}{\partial x_i}\right)$$

and < > denotes the average over a plane parallel to the walls. The small-scale eddy viscosities ν_T and $\overset{*}{\nu}_T$ represent the action of the unresolved scales of motion on those that are resolved. Hence, as the resolution gets better, ν_T and $\overset{*}{\nu}_T$ should get smaller. Since the filter widths represent the largest length scales that are __not__ resolved, these widths are the characteristic size of the largest (and hence most important) residual motions.

The first term in (3.1) with

$$\nu_T = (C_s \Delta)^2 \sqrt{2(S_{ij} - \langle S_{ij} \rangle)(S_{ij} - \langle S_{ij} \rangle)} \tag{3.2}$$

is Smagorinsky's model and can be derived from equating the subgrid scale (SGS) production and dissipation in homogeneous turbulence. This model was used successfully in the numerical simulation of the decay of isotropic turbulence by Mansour et al. (1977) and by Deardorff (1970) (with $S_{ij} - \langle S_{ij} \rangle$ replaced by S_{ij}) in the calculation of the core region of turbulent channel flow. In the expression for ν_T (Eq. (3.2)), Δ is the characteristic length scale of the largest subgrid scale eddies, here assumed to be (Deardorff, 1970)

$$\Delta = (\Delta_1 \Delta_2 \Delta_3)^{1/3} \tag{3.3}$$

C_s is a dimensionless constant, and Δ_i is the filter width in the i-direction. In addition, in order to account for low Reynolds number SGS turbulence near the wall, the above expression for Δ was multiplied by the Van Driest (1956) exponential damping function, $1 - \exp(-y^+/A^+)$, with $A^+ = 25$ and $y^+ = y_w u_\tau / \nu$, the distance to the nearest wall in the wall units. In all the calculations reported here which were performed with different grid sizes, the value of $C_s = 0.065$ was used. Numerical experiments indicated that the use of a value much larger than this one resulted in excessive

9

damping of the resolvable turbulence. When lower values of C_s were used, excess energy accumulated near the high wave number end of one-dimensional energy spectra. In general, however, the computed turbulence intensities were rather insensitive to small perturbations ($\approx 20\%$) of C_s. Note that the above value of C_s corresponds to $C_s = 0.1$, used by Deardorff (1970), if Δ_i in (3.3) is replaced by h_i.

Near the wall the important large scale structures are the "streaks" (Kline et al., 1967). These structures are relatively finely spaced in the spanwise direction. Their mean spacing characterizes the length scale of the eddies in the viscous sublayer (and hence the thickness of the viscous sublayer). Thus in a calculation with inadequate resolution in the spanwise direction, the thickness of the viscous sublayer will probably be larger than its physical counterpart. This in turn will lead to lower gradients of the computed mean velocity profile and consequently insufficient production of the resolvable turbulent kinetic energy. Therefore, in order to account for the effect of some of the streaks that reside in SGS motion on the mean velocity profile, the second term in (3.1) was introduced in the model for τ_{ij}. As was mentioned earlier, Schumann (1975) has also decomposed SGS stresses into two parts, as in (3.1). The first was to account for locally isotropic SGS stresses, and the second to account for inhomogeneities due to the nonzero component of mean strain.

In the present study, the eddy viscosity, v_T^*, is defined as follows:

$$v_T^* = c(D\Delta_3)^2 \sqrt{2 \langle S_{ij} \rangle \langle S_{ij} \rangle} \tag{3.4}$$

where $c = 0.065$ is a dimensionless constant and $D = 1 - \exp(-y^{+2}/A^{+2})$ is a wall-damping function with $A^+ = 25$, as before. It should be pointed out that the characteristic length scale associated with v_T^* is Δ_j, the filter

10

width in the spanwise direction. As the resolution in the z-direction is improved, v_T^* will approach zero. Moreover, it should be noted that, due to its functional form (function of y only), $v_T^{\ddot{}}$ does not appear directly in the governing equations for the resolvable portions of turbulence stresses and hence does not contribute to the dissipation terms in these equations. This is in contrast to v_T, which will supplement the molecular viscosity as a dissipating agent for the resolvable turbulence stresses. However, v_T^* contributes to the dissipation of mean kinetic energy, $\frac{1}{2}<\bar{u}>^2$, and therefore indirectly to the production of resolvable turbulence stresses. The value of c in Eq. (3.4) was chosen to be 0.065 from a numerical experiment. It is approximately the minimum value with which the resolvable turbulent kinetic energy can be maintained (i.e., it did not decay indefinitely). This numerical experiment was performed with one of the computations reported in Table 1 (Case 1), but the same constant was used in all the other calculations reported here.

4. The Computational Grid

Three factors influence the choice of the computational grid. First, the mesh size should be small enough to resolve the important scales of motion in the flow. Second, the computational domain should be large enough that artificialities of the boundary conditions do not influence the statistics of the solution in an undesirable way. Third, the availability of computer resource restricts the size of calculation that can be done.

In the direction normal to the walls $(-1 \leq y \leq 1)^\dagger$ 63 grid points with non-uniform spacings were distributed. The following transformation gives the location of grid points in this direction:

---

†For notational simplicity, we occasionally shift from (x_1,x_2,x_3), (u_1,u_2,u_3) to (x,y,z), (u,v,w).

$$y_j = \frac{1}{2} \tanh\left[\xi_j \tanh^{-1}(a)\right] \tag{4.1}$$

where

$$\xi_j = -1 + 2(j-1)/(N_2 - 1) \quad , \quad j = 1, 2, \ldots, N_2$$

N_2 is the total number of grid points in the y-direction. Here a is the adjustable parameter of the transformation $(0 < a < 1)$; a large value of a distributes more points near the walls. In our computations we have used $a = 0.98346$, $N_2 = 63$. This value of a was selected so that the above grid distribution in the y-direction is sufficient to resolve the viscous sublayer $(y^+ < 5)$.

The selection of the length of the computational box in the streamwise and spanwise directions is initially guided by the two-point correlation measurements of Comte-Bellot (1963). Her data show that the correlation between velocity fluctuations at two points away from the walls[*] separated in x_1 becomes negligible at an x_1 separation of 3.2δ. The correlation between motions at two points (away from the walls) separated in x_3 becomes negligible beyond an x_3 separation of 1.6δ. thus, if we wish to employ periodic boundary conditions in x_1 and x_3 directions, we must choose a computational domain approximately twice as large as these dimensions. This is to prevent these simple but artificial boundary conditions from seriously influencing the results (Schumann, 1973). It should be noted, however, that the computed two-point correlation functions provide sufficient information regarding the adequacy of the computational domain. If, for example, in the x_1-direction the length of the computational box, L_1, is too short, the computed profile(s) of $R_{11}(y,r)$ does not decay sufficiently in the neighborhood of $r = L_1/2$, and hence L_1 should be increased.

---

[*]Near the wall data are not available.

In the wall region, the important large-scale structures are the "streaks" (Kline et al., 1967). These have a mean spanwise spacing corresponding to $\lambda_{3m}^{+} \approx 100$, with the most probable spanwise spacing, λ_{3p}^{+}, about 80 in the wall units. In addition, Kline et al. (1967) and Clark and Markland (1970) occasionally observed U-shaped vortices in the inner region. In the studies of Clark and Markland, the average streamwise spacing of these structures was found to be $\lambda_{1m}^{+} = 440$. For the present computation at $Re_\tau \approx 640$, these correspond to dimensionless spacings of

$$\lambda_{1m} = 440/640 = 0.687$$

$$\lambda_{3p} = 80/640 = 0.125$$

Table 1 shows the characteristics of the computational grid networks in four different calculations reported here. In this table, N_i is the number of grid points; L_i is the length of the computational box, h_i is the grid spacing in the i-direction, and subscripts 1 and 3 refer to the streamwise and spanwise directions, respectively. The L_1/δ and L_3/δ entries in Table 1 show that, except for case 1, where $L_3 < 3.2\delta^{\dagger}$, the size of the computational domain in all other cases appears to be large enough to accommodate the important large eddies. Furthermore, since the pseudospectral method (Section 5) is used to approximate the derivatives in the streamwise and spanwise directions, the computational grid resolution (at least for Cases 2, 3, and 4) appears to be just adequate to resolve structures with λ_{1m} and λ_{3p} spacing in the x_1- and x_3-directions, respectively. It is emphasized that the above values for λ_{1m} and λ_{3p} are based on an ensemble of measurements, and, at a given instant, structures with a finer spacing than λ_{3p} and λ_{1m} can be

---

†In this case, the computed two-point correlation functions $R_{33}(y, r_3)$ (for $y > .2\delta$) indicate that L_3 is not sufficiently long.

formed which cannot be resolved with the current grid resolution. Thus, we cannot expect the present calculations to reveal the streaky structures in the viscous sublayer with _mean_ spacing equal to λ_{3m}. As we shall see, however, calculations do produce streaks at the finest scale permitted by the grid.

Finally, we mention that the grid meshes for pressure do not coincide with grid meshes for velocities. Grid points for P are located midway between those for $\overline{u}_1$. The equation of continuity is enforced at node points for P, whereas the momentum equations are evaluated at node points for $\overline{u}_1$. Note that, in contrast to the conventional staggered grid system (Harlow and Welch, 1965), in which the three velocity components are defined at different node points, in the present grid system all the velocities are defined at the same grid points. This will allow for convenient application of the wall boundary conditions.

5. The Numerical Method

Partial derivatives in the x_1 and x_3 directions were evaluated pseudospectrally (Orszag, 1972). This involves taking the x_1 (or x_3) Fourier transform of the function to be differentiated, multiplying the result by ik_1 (or ik_3), where k_1 (k_3) is the wavenumber in the x_1 (x_3) direction, followed by inverse transformation to get the desired derivative. This method has the advantage that it handles the high wavenumber components of the function precisely. Thus, the use of the pseudospectral method in the x_1 and x_3 directions gives us the best possible resolution (with a given number of grid points) in these directions. Partial derivatives in the x_2 direction were approximated by central difference formulae. These will be described below.

The time advancement was made using a semi-implicit method (Moin et al., 1978). The momentum equations (2.6) were recast in the form

$$\frac{\partial \bar{u}_1}{\partial t} = -\frac{\partial P}{\partial x_1} + \left[(1 + \delta_{12}) < \nu_T > + \delta_{11} \nu_T^* + \frac{1}{Re_\tau} \right] \frac{\partial^2 \bar{u}_1}{\partial x_2^2}$$

$$+ \frac{1}{Re_\tau} \left(\frac{\partial^2 \bar{u}_1}{\partial x_1^2} + \frac{\partial^2 \bar{u}_1}{\partial x_3^2} \right) + H_1 \quad \text{(no summation)}$$

(5.1)

where H_1 contains all of the terms in (2.6) that are not in (5.1). For discretization in time, we used the Adams-Bashforth method for H_1 and the Crank-Nicolson method for the remaining terms in the right-hand side of Eq. (5.1). For convenience, we evaluated $< \nu_T >$ and ν_T^* at the old time step n.

In Eq. (5.1), H_1 includes the term

$$\overline{\epsilon_{ijk} \bar{u}_j \bar{\omega}_k + \frac{\partial}{\partial x_j} \frac{1}{2} \bar{u}_j \bar{u}_j}$$

The computation of this term can be accomplished by first calculating the term under the large overbar, taking the Fourier transform with respect to x_1 and x_3, multiplying by the Fourier transform of the Gaussian filter function, and then inverse transforming.

Next, we Fourier transform the resulting equations in the x_1 and x_3 directions. this converts the set of partial differential equations (5.1) to the following system of ordinary differential equations, for every pair of Fourier modes k_1 and k_3 with $y = x_2$ as the independent variable:

$$\frac{\partial^2 \hat{u}_1^{n+1}}{\partial y^2} + \beta_1 \left[1 + \frac{\Delta t}{2Re} (k_1^2 + k_3^2) \right] \hat{u}_1^{n+1} + ik_1 \beta_1 \frac{\Delta t}{2} \hat{P}^{n+1} = \hat{Q}_1 \quad \text{(5.2a)}$$

$$\frac{\partial^2 \hat{u}_2^{n+1}}{\partial y^2} + \beta_2 \left[1 + \frac{\Delta t}{2Re} (k_1^2 + k_3^2) \right] \hat{u}_2^{n+1} + \beta_2 \frac{\Delta t}{2} \frac{\partial \hat{P}^{n+1}}{\partial y} = \hat{Q}_2 \quad \text{(5.2b)}$$

$$\frac{\partial^2 \hat{u}_3^{n+1}}{\partial y^2} + \beta_3 \left[1 + \frac{\Delta t}{2Re} (k_1^2 + k_3^2) \right] \hat{u}_3^{n+1} + ik_3 \beta_3 \frac{\Delta t}{2} \hat{P}^{n+1} = \hat{Q}_3 \quad \text{(5.2c)}$$

Here, $\beta_i (i = 1,2,3)$ are known functions of Re_τ, $< v_T >^n$, and v_T^{*n} and $\hat{Q}_i$ represent the terms involving pressure and velocity field at time steps n and $n - 1$.

The following central difference formulae,

$$\frac{\partial^2 f}{\partial y^2}\bigg|_j \simeq 2\left[\frac{f_{j-1}}{h_j(h_j + h_{j+1})} - \frac{f_j}{h_j h_{j+1}} + \frac{f_{j+1}}{h_{j+1}(h_j + h_{j+1})}\right] \qquad (5.3a)$$

$$\frac{\partial f}{\partial y}\bigg|_q \simeq \frac{f_{q+1} - f_q}{y_{q+1} - y_q} \qquad (5.3b)$$

were used to approximate

$$\frac{\partial^2 \hat{u}_i^{n+1}}{\partial y^2} \quad \text{and} \quad \frac{\partial \hat{P}^{n+1}}{\partial y}$$

respectively, in Eqs. (5.2). Here j denotes the velocity mesh point y_j, q the pressure mesh point y_q, and $h_j = y_j - y_{j-1}$. The resulting set of equations, together with the equation of continuity evaluated at the pressure node points,

$$\frac{ik_1}{2}\left(\hat{u}_{1_{j+1}}^{n+1} + \hat{u}_{1_j}^{n+1}\right) + \frac{\hat{u}_{2_{j+1}}^{n+1} - \hat{u}_{2_j}^{n+1}}{h_{j+1}} + \frac{ik_3}{2}\left(\hat{u}_{3_{j+1}}^{n+1} + \hat{u}_{3_j}^{n+1}\right) = 0 \qquad (5.4)$$

leads to a system of algebraic equations for the Fourier transform of the dependent variables at the new time step. This system is of block-tridiagonal form and can be solved very efficiently (see below). No-slip boundary conditions on velocity were used at the walls $(y = \pm 1)$ and periodic boundary conditions were incorporated in the x_1 and x_3 directions. Note that pressure wall conditions are not necessary; only velocity boundary conditions are sufficient to close the system of equations (see Moin and Kim, 1980).

In the present calculations, the core memory of the ILLIAC IV is large enough to hold only a few planes of the dependent variables. Therefore, it is

important to manage efficiently the transfer of data between the core and disk memory, where the entire data base resides. A detailed description of the data-management technique used here is given in Kim and Moin (1979). Here, we briefly outline the essential steps. At each time step, the system of algebraic equations just described is solved by two separate passes through the data base. In PASS 1, the right-hand side of these equations is computed. This is accomplished by transferring two (x-z) planes of the independent variables from the disk memory to the core memory to be processed by a double-buffer scheme. In this manner, all the (x-z) planes are transferred to the core, two planes at a time.

In PASS 2, the block-tridiagonal system must be solved for each k_1 and k_3. In this pass, (y-k_3) planes of the right-hand side vector that were computed in PASS 1 are transferred to the core memory. Due to the limitation of the core size of the ILLIAC IV, a special algorithm had to be developed to solve the block-tridiagonal system of equations. For each k_1 and k_3, this algorithm requires $676 N_2$ floating-point arithmetic operations, in contrast to $376 N_2$ operations for the conventional block-tridiagonal solver (Merriam, 1978). The extra computations are necessary in order to avoid the extra I/O passes that would otherwise have been necessary.

With a full use of the parallel processing capabilities of the ILLIAC IV computer and the above data-management technique, the computer time per time step (CPU and I/O time) was 22 sec for $63 \times 64 \times 64$ grid-point calculations and 36 sec for the computations with $63 \times 64 \times 128$ grid points. For the calculations shown in Table 1, the dimensionless time step, Δt, was set at 0.001 for Case 1, 0.00075 for Case 2, and 0.0005 for Cases 3 and 4. Throughout the computations, the value of

$$C(t) = \text{Max} \left\{ \Delta t \left[\left| \frac{\bar{u}}{h_1} \right| + \left| \frac{\bar{v}}{h_2(y)} \right| + \left| \frac{\bar{w}}{h_3} \right| \right] \right\}$$

never exceeded 0.35.

17

The initial condition for Case 1 in Table 1 was obtained by assigning the final velocity field described in Kim and Moin (1979) to the corresponding grid points used here. For Case 2, the final velocity field from Case 1 was simply assigned to the alternate mesh points. The values at the intermediate points were obtained by Fourier interpolation. A similar procedure was used to generate the initial velocity field for Cases 3 and 4.

6. Mean Velocity Profile and Turbulence Statistics

Starting from the initial velocity field, for each case, the governing equations were integrated forward in time until the numerical solutions reached statistically steady states. These equilibrium states were identified by approximate periodicity of the horizontally averaged turbulence stresses in time. Next, in order to obtain better statistical samples, the equations were further integrated in time and a running time average of the horizontally averaged turbulence quantities was calculated. For each case, the calculations were considered to be complete when the time-averaged turbulence quantities became stationary. The total time of integration and the averaging time for all the computations reported here are shown in Table 1.

Figure 1 shows the mean velocity profile $< \bar{u} >$ (unless otherwise stated in this section, $< \ >$ indicates horizontal as well as time averaging) for all cases reported in Table 1. The calculated mean velocity profiles are in good agreement with each other as well as with the experimental data of Hussain and Reynolds (1975). It appears that, at least for the different computational grid networks considered here, the law of the wall and the corresponding logarithmic layer and von Kármán constant can be predicted with virtually no dependence on the grid resolution. This is particularly significant in light of the fact that the characteristic length scale of the subgrid

18

scale model used here is a function of computational grid resolution. Figure 2 shows the profiles of the correlation coefficient between the resolvable streamwise and vertical components of turbulence fluctuations,

$$< \overline{u'' v''} > / [< \overline{u''^2} >^{1/2} < \overline{v''^2} >^{1/2}]$$

where $\overline{u''} = \overline{u} - < \overline{u} >$. The calculated profiles for all the cases reported in Table 1 are in good agreement with each other and with the experimental data of Sabot and Comte-Bellot (1976). The results presented in Fig. 2 together with those in Fig. 1 establish some confidence in the reliability of the sub-grid scale model used in this study.

In the remainder of this paper we shall present, in some detail, the results obtained from Case 4 in Table 1. The computational grid resolution for this case is better than for all the other cases; and, as will be shown later in this section, the computational domain appears to be large enough to include the important large eddies.

6.1. Turbulence Stresses

Vertical profiles of the resolvable mean Reynolds shear stress, $< \overline{u'' v''} >$, and the total Reynolds shear stress, $< \overline{u'' v''} > + < \tau_{12} >$, are shown in Fig. 3. These profiles indicate that the average Reynolds shear stress profile has attained the equilibrium shape which balances the downstream mean pressure gradient in the regions away from the walls. In the vicinity of the walls, the viscous stresses are significant, and they, together with the total Reynolds stress, balance the mean pressure gradient. The symmetry of the $|< \overline{u'' v''} > + \tau_{12}|$ profile about the channel centerline indicates that the total averaging time and statistical sample are adequate. Moreover, it should be noted that the subgrid-scale contribution to the total Reynolds stress is significant only in the vicinity of the walls.

19

Figures 4 and 5 show the profiles of the dimensionless resolvable turbulence intensities. For comparison, some of the available experimental data over a range of Reynolds numbers are also shown. Once again, the symmetry of the calculated turbulence intensities about the centerline of the channel indicates that the total averaging time was sufficient for an adequate statistical sample. The overall agreement of the computed turbulence intensities with the experimental measurements is good. In Fig. 5, the resolvable turbulence intensities in the vicinity of the lower wall are plotted vs. $y^+ = y_w u_\tau / \nu$. In spite of large differences among various measurements, the maximum of the computed $< \overline{u}''^2 >^{1/2}$ is located at a distance farther away from the wall ($y^+ \simeq 30$) than those of the measured turbulence intensities ($y^+ \simeq 13$-20). In addition, in the immediate neighborhood of the wall, an appreciable fraction of the vertical component of turbulence intensity appears to reside in the subgrid-scale motions. It should be noted that, in contrast to the turbulence shear stress, in order to deduce the subgrid scale contribution to turbulence intensities one has to obtain an estimate for the kinetic energy of SGS stress, Q_{kk}, and use it in Eq. (2.8a). Due to the high degree of anisotropy in the channel flow, especially in the vicinity of the walls, we have been unable to obtain a reasonably accurate estimate for Q_{kk}.

6.2. Two-Point Correlation Functions

Two-point correlation functions

$$R_{11}(y,r_1) = \frac{< \overline{u}''_1(x,y,z)\, \overline{u}''_1(x + r_1,y,z) >}{< \overline{u}''^2_1(x,y,z) >}$$

and

$$R_{11}(y,r_3) = \frac{< \overline{u}''_1(x,y,z)\, \overline{u}''_1(x,y,z + r_3) >}{< \overline{u}''^2_1(x,y,z) >}$$

for $i = 1,2,3$ (no summation) are plotted in Figs. 6 and 7 at four vertical locations. These profiles show that in general, for small separation distances, the correlation for the velocity in the direction of the displacement is larger than the corresponding transverse correlations. In addition, the longitudinal correlation in the streamwise direction extends over much longer distances than do all other correlations. This result was also obtained by Deardorff (1970).

The slow decay of $R_{11}(y_w = 0.025, r_1)$ for increasing r_1 indicates that near the wall the eddies are highly elongated in the streamwise direction. On the other hand, the profiles of $R_{11}(y,r_3)$ show that the spanwise extent of turbulence structures near the wall is much smaller than for those away from the wall. Thus, it appears that, in accordance with the experimental observations, near the walls the computed flow field consists of elongated streaky structures. The structure of the flow field will be examined in some detail in the next section.

For comparison, in Figs. 6 and 7, the profiles of $R_{11}(y_w,r_1)$ $(i = 1,3)$ at $y_w/\delta = 0.11$, 0.44, and 1.0 from Comte-Bellot's (1963) measurements are included. Note that the computed and measured correlations are obtained at slightly different vertical locations. The correlations were calculated at selected points in the y-direction, and the comparison is made at the locations where the y-coordinate of the computed and measured correlations were closest to each other. For small values of the non-dimensionalized separation distance, r_1, the measured correlations, $R_{11}(y_w,r_1)$, are smaller than the computed ones, whereas for larger values of r_1 the reverse is true. At small values of r_1, the discrepancy between the computed and measured correlations is due to the fact that the measurements were made at a much larger Reynolds number (Re = 135,000) than in the present simulation (see

Batchelor, 1953). However, the cause of the difference between the computed and measured profiles for larger values of r_1 is not clear. Comparison of the measured profiles with the computed ones obtained from calculations with larger computational box lengths in the streamwise direction shows no improvement. Thus, the streamwise extent of the computational box does not appear to be a factor here. However, possible inadequate resolution in the x-direction may suppress the formation of some small scale structures. In this case, these structures could conceivably combine to form eddies that have long streamwise extent throughout the channel cross section. In addition, it should be mentioned that Comte-Bellot's axial two-point correlation data were obtained by traversing one probe downstream of another probe. With this procedure, the measured $R_{11}(y,r_1)$ may be contaminated with errors, due to the effect of the wake of the upstream probe. However, the probe interference effect should be significant only for small separation distances.

In Fig. 7, the profiles of $R_{11}(y_1 r_3)$ are also compared with the measurements of Comte-Bellot. Aside from the Reynolds number effect for small values of r_3, the agreement between the computed and measured correlations is good. Finally, the other two spanwise correlations, $R_{22}(y,r_3)$ and $R_{33}(y,r_3)$, were also compared with the corresponding ones measured by Comte-Bellot. The measured $R_{22}(y,r_3)$ and $R_{33}(y,r_3)$ are systematically lower than the computed ones for the values of r_3 for which these correlations have appreciable magnitude.

6.3. Skewness and Flatness Factors of Resolvable Turbulence

The velocity skewness and flatness factors which are defined as

$$S(\overline{u}''_i) = \frac{\langle \overline{u}''^3_i \rangle}{\langle \overline{u}''^2_i \rangle^{3/2}} \quad \text{and} \quad F(\overline{u}''_i) = \frac{\langle \overline{u}''^4_i \rangle}{\langle \overline{u}''^2_i \rangle^2} \quad (i = 1,2,3; \text{ no summation})$$

respectively, are plotted in Fig. 8. The flatness factors of all the velocity components reach their maxima at the wall. This indicates that in the vicinity of the wall the turbulence is highly intermittent. Throughout an appreciable portion of the channel cross section, $F(\overline{u}_3)$ and $S(\overline{u}_3)$ are approximately equal to three and zero, respectively. These values correspond to the flatness and skewness factors of a Gaussian distribution. However, Kreplin and Eckelmann (1979) measured the u_3 probability distribution and have shown that it is not Gaussian, even though the values of $S(u_3)$ and $F(u_3)$ correspond to that of a Gaussian distribution.

Near the wall, $S(\overline{u}''_i)$ is positive, whereas away from the wall it is negative. This indicates that near the wall the large-amplitude $\overline{u}$ fluctuations are primarily due to arrival of high-speed fluid from regions away from the wall. On the other hand, away from the wall the large-amplitude $\overline{u}$ fluctuations are most probably associated with low-speed fluid leaving the wall region. These observations are in agreement with the experimental findings of Brodkey et al. (1974) and with contour plots of $\overline{u}''\overline{v}$ from numerical simulation of turbulent channel flow (Kim and Moin, 1979). However, as will become clear below, the precise vertical location (in wall units) of the crossover point in the present calculation is in disagreement with experimental data. This discrepancy is probably due to inadequate grid resolution in the computations.

In Fig. 8, the profiles of skewness and flatness factors from measurements of Comte-Bellot (1963) and Kreplin and Eckelmann (1979) are reproduced.

The overall agreement between computational and experimental data is good. This is particularly encouraging considering the significant contribution of small scale turbulence to these quantities and the difficulties associated with their measurements.

6.4. Resolvable Vorticity Fluctuations

Figure 9 shows the profiles of the non-dimensional rms vorticity fluctuations. The spanwise component of vorticity fluctuations, $< \omega_3''^2 >^{1/2}$, attains its maximum at the wall and decreases monotonically towards the channel centerline. The profile of the rms streamwise vorticity fluctuations, $< \omega_1^2 >^{1/2}$, also attains its maximum at the wall but, in addition, displays a local maximum at $y^+ \approx 30$. At about the same location, the peak of the rms vertical component of the vorticity is located. The mechanics underlying this behavior of the profile of $< \omega_1^2 >^{1/2}$ will be discussed in the next section.

It is interesting to note that, in spite of large differences between different components of rms $< \omega_1''^2 >^{1/2}$ near the wall, away from the wall $(y^+ > 70)$ they are virtually identical. This is in contrast to rms velocity fluctuations, $< \overline{u_1''^2} >^{1/2}$. The difference between the two may be explained by noting that the relative contribution of small scales to vorticity fluctuations is significantly larger than their contribution to velocity fluctuations, and away from the walls the small scales tend to be isotropic. Exploiting the "isotropy" of vorticity fluctuations may be very useful in statistical analysis of turbulent shear flows.

The limiting wall value of vorticity fluctuations in the present calculations are 0.20 τ_w and 0.13 τ_w for $< \omega_3''^2 >^{1/2}$ and $< \omega_1^2 >^{1/2}$, respectively. The agreement of these computed values with experimental measurements (see Kreplin and Eckelmann, 1979, for data from several measurements) is satisfactory.

6.5. Statistics Involving Resolvable Pressure Fluctuations

The root-mean square value of the resolvable wall pressure fluctuations, $< p^2 >^{1/2}/\tau_w$, is 2.05 for both walls. This value is in fair agreement with the values of 2.64 obtained by Willmarth and Wooldridge (1962), 2.31 by Willmarth (1965), 2.6 by Elliot (1972), and of 2.0 and 2.5 reported by Corcos (1962) for fully developed pipe flows. However, the computed values are considerably lower than the 3.59 obtained by Blake (1970) or Emmerling's (1973) measurements (see Willmarth (1975)).[*] The measurements of Blake and Emerling were made with a pinhole microphone and by optical techniques, respectively. Therefore, in these experiments the smaller-scale pressure variations are expected to be better resolved. Thus, in view of these two experiments, it appears that an appreciable portion of the pressure fluctuations may reside in subgrid scale motions.

The profiles of the diagonal elements of the **resolvable** pressure strain correlation tensor

$$\phi_{ij} = < p \left(\frac{\partial \bar{u}_i}{\partial x_j} + \frac{\partial \bar{u}_j}{\partial x_i} \right) >$$

are shown in Figs. 10 and 11. These terms govern the exchange of energy between the three components of resolvable turbulence kinetic energy (Hinze, 1975). The negative sign for $\phi_{\ell\ell}$ (no summation) indicates loss, or transfer of energy from $< \bar{u}_\ell^2 >^{1/2}$ to other components, whereas a positive sign denotes energy gain. These profiles show that, except in the close vicinity of the wall, as expected, the streamwise component of turbulent velocity fluctuations transfers energy to the cross stream components. However, very near the wall, there is a large transfer of energy from the vertical component

---

[*] See Willmarth (1975) for the above references, as well as values from other sources.

of turbulence intensity to the horizontal components. In this work, we shall refer to this phenomenon as the "splatting" effect. It will be shown that the splatting effect is an important property of the flow in the vicinity of the walls and should be taken into account in the modeling of near-wall turbulence. In fact, this phenomenon was noted in a previous study by Daly and Harlow (1970), who included a term in their statistical model of ϕ_{ij} to account for its effect.

The profile of the off-diagonal element ϕ_{12}, together with the pressure diffusion term $-\frac{\partial}{\partial y} \langle \overline{P u}'' \rangle$ and their sum

$$P_{uv} = - \langle \overline{u}'' \frac{\partial P}{\partial y} + \overline{v} \frac{\partial P}{\partial x} \rangle$$

in the vicinity of the lower wall are shown in Fig. 12. The last term, P_{uv}, appears in the governing equation for resolvable turbulence shear stress, $\langle \overline{u}'' \overline{v} \rangle$. The components of P_{uv}, ϕ_{12}, and $-\frac{\partial}{\partial y} \langle \overline{P u}'' \rangle$, have comparable magnitudes and, as will be shown below, near the wall they provide important contributions to the governing equation for $\langle \overline{u}'' \overline{v} \rangle$. As expected (Hinze, 1975), except in the immediate neighborhood of the wall, the sign of ϕ_{12} is opposite to that of $\langle \overline{u}'' \overline{v} \rangle$. However, near the wall, where the splatting effect is present, ϕ_{12} has the same sign as $\langle \overline{u}'' \overline{v} \rangle$, thus contributing to the production of turbulence.

6.6. Resolvable Turbulence Intensity and Shear Stress Balance

In phenomenological turbulence modeling, the objective is to construct rational models for the correlations that appear in the governing equations for the Reynolds stresses. For the resolvable portion of the flow field in channel flow, these equations are:

26

$$\frac{\partial \langle \overline{u}_1^{"2} \rangle}{\partial t} = - \langle \overline{u}_1^{"} \overline{u}_2 \rangle \frac{\partial \langle \overline{u} \rangle}{\partial x_2} - \frac{\partial}{\partial x_2} \langle \overline{u}_1^{"2} \overline{u}_2 \rangle - 2 \langle \overline{u}_1^{"} \frac{\partial P}{\partial x_1} \rangle + \qquad (6.1)$$

$$\frac{\partial}{\partial x_2} \langle (\nu_T + \frac{1}{Re}) \frac{\partial \overline{u}_1^{"2}}{\partial x_2} \rangle - 2 \langle \overline{u}_1^{"} \frac{\partial}{\partial x_j} \lambda_{1j} \rangle - 2 \langle (\frac{1}{Re} + \nu_T) \frac{\partial \overline{u}_1^{"}}{\partial x_j} \frac{\partial \overline{u}_1^{"}}{\partial x_j} \rangle + A_{11}$$

$$\frac{\partial \langle \overline{u}_2^2 \rangle}{\partial t} = - \frac{\partial}{\partial x_2} \langle \overline{u}_2^3 \rangle - 2 \langle \overline{u}_2 \frac{\partial P}{\partial x_2} \rangle + \frac{\partial}{\partial x_2} \langle (\nu_T + \frac{1}{Re}) \frac{\partial \overline{u}_2^2}{\partial x_2} \rangle$$

$$\qquad (6.2)$$

$$- 2 \langle \overline{u}_2 \frac{\partial}{\partial x_j} \lambda_{2j} \rangle - 2 \langle (\frac{1}{Re} + \nu_T) \frac{\partial \overline{u}_2}{\partial x_j} \frac{\partial \overline{u}_2}{\partial x_j} \rangle + A_{22}$$

$$\frac{\partial \langle \overline{u}_3^2 \rangle}{\partial t} = - \frac{\partial}{\partial x_2} \langle \overline{u}_3^2 \overline{u}_2 \rangle - 2 \langle \overline{u}_3 \frac{\partial P}{\partial x_3} \rangle + \frac{\partial}{\partial x_2} \langle (\nu_T + \frac{1}{Re}) \frac{\partial \overline{u}_3^2}{\partial x_2} \rangle$$

$$\qquad (6.3)$$

$$- 2 \langle \overline{u}_3^{"} \frac{\partial}{\partial x_j} \lambda_{3j} \rangle - 2 \langle (\frac{1}{Re} + \nu_T) \frac{\partial \overline{u}_3}{\partial x_j} \frac{\partial \overline{u}_3}{\partial x_j} \rangle + A_{33}$$

$$\frac{\partial \langle \overline{u}_1^{"} \overline{u}_2 \rangle}{\partial t} = - \langle \overline{u}_2^2 \rangle \frac{\partial \langle \overline{u} \rangle}{\partial y} - \frac{\partial}{\partial x_2} \langle \overline{u}_1^{"} \overline{u}_2^2 \rangle - \langle \overline{u}_1^{"} \frac{\partial P}{\partial x_2} + \overline{u}_2 \frac{\partial P}{\partial x_1} \rangle$$

$$+ \frac{\partial}{\partial x_2} \langle (\nu_T + \frac{1}{Re}) \frac{\partial \overline{u}_1^{"} \overline{u}_2}{\partial x_2} \rangle - \langle \overline{u}_1^{"} \frac{\partial}{\partial x_j} \lambda_{2j} + \overline{u}_2 \frac{\partial}{\partial x_j} \lambda_{1j} \rangle$$

$$- 2 \langle (\frac{1}{Re} + \nu_T) \frac{\partial \overline{u}_1^{"}}{\partial x_j} \frac{\partial \overline{u}_2}{\partial x_j} \rangle + A_{12} \qquad (6.4)$$

It should be emphasized that the above equations are for the resolvable portion rather than the total turbulent stresses. However, considerable insight into the mechanics of energy transfer and the relative importance of various terms in the Reynolds stress equations may be gained from the corresponding terms in these equations.

In Figs. 13-17, all the correlations appearing in the above equations, and in the governing equation for the resolvable turbulent kinetic energy, $q^2 = \frac{1}{2} \langle \overline{u}_1^{"} + \overline{u}_2^2 + \overline{u}_3^2 \rangle$, are plotted in the vicinity of the lower wall (y^+ < 90). The first term in the right-hand side of Eqs. (6.1) and (6.4) is the

27

production term. In Figs. 13-17, the remaining five terms in the right-hand side of each equation are labeled as convection, velocity-pressure gradient (VPG), diffusion, cascade, and dissipation. The last term in each equation, A_{ij}, is a relatively complicated expression involving ν_T. They would be identically equal to zero if ν_T were a constant. These terms were calculated and found to be negligibly small compared to the other terms in each equation.

In Figs. 13 and 17, the production and dissipation are clearly the dominant terms in most of the region shown. In the immediate neighborhood of the wall, however, where the production term is small, viscous diffusion carries sufficient energy inward to balance the large viscous dissipation there. In addition, it can be seen that, aside from the close vicinity of the wall ($y^+ < 15$), energy is convected from the wall region, where production is high, to the regions away from the wall.

The velocity-pressure gradient terms make large contributions to the balance of the governing equations for normal and spanwise components of turbulent kinetic energy. Near the wall, the triple correlation term (convection) and pressure strain and pressure diffusion terms in the $< \overline{u_2^2} >$ equation are very significant. In particular, the reduction of the normal component of turbulent energy due to the splatting effect mentioned above is compensated by the pressure diffusion term.

Near the wall ($y^+ < 25$), in the dynamical equation for Reynolds shear stress, $< \overline{u''v} >$, the triple correlation and velocity-pressure gradient, P_{uv}, are the dominant terms. However, for $y^+ > 25$, the contribution of P_{uv} is small and the production term takes on a more active role. Moreover, it should be noted that in this equation the viscous diffusion and "dissipation" terms appear to be negligible. This in turn implies that the governing equation for $< \overline{u''v} >$ has a hyperbolic character.

28

In Eqs. (6.2)-(6.4) and in Figs. 13-17, the terms involving molecular and eddy viscosity were combined. In Fig. 18, the dissipation of turbulent kinetic energy due to molecular and eddy viscosity are plotted separately. It can be seen that, near the wall, the dissipation due to eddy viscosity is negligible compared to that due to molecular viscosity. However, in the regions away from the wall, they are comparable. Finally, in Fig. 18, the cascade term, $- \langle \overline{u}_i'' \frac{\partial}{\partial x_j} \lambda_{ij} \rangle$, is also plotted. Near the wall, its magnitude is larger than the dissipation due to eddy viscosity, and away from the wall they are of the same order of magnitude. Therefore, as was pointed out in Sect. 2, inclusion of $\langle \overline{u}_i'' \frac{\partial}{\partial x_j} \lambda_{ij} \rangle$ in the modeling assumption for the subgrid scale stresses is not recommended. As long as this term can be evaluated explicitly, one should do so.

7. Detailed Flow Structures

In this section we shall investigate the detailed structure of the computed flow field. This will be done by examining contour plots of instantaneous velocity, pressure, and vorticity field, and by tracking passive particles in the flow. The latter approach is a simulation of laboratory flow-visualization experiments using hydrogen-bubble wire.

Figure 19 shows the contour plot of $\overline{u}''$ in the x-z plane at $y^+ = 6.26$ and at the non-dimensional time, $t = 4.3$. In all the contour plots shown here, positive values are contoured by solid lines and negative values are contoured by dashed lines. In addition, all the instantaneous plots are obtained at the non-dimensional time $t = 4.3$. The distinct feature of the flow patterns in Fig. 19 is the existence of highly elongated regions of high-speed fluid $(\overline{u}'' > 0)$ located adjacent to the low-speed regions. This picture of the flow in the vicinity of the wall is in agreement with laboratory observations. In their visual studies, Runstadler et al. (1963) and, more

29

recently, other investigators have clearly demonstrated that the viscous sublayer consists of coherent structures of high- and low-speed streaks alternating in the spanwise direction. These studies have also shown that the streaks are the unique characteristic of the wall-layer turbulence, and they are absent in the regions away from the walls. Figure 20 shows the contour plot of $\overline{u}$ in an x-z plane far away from the wall ($y^+ = 400$). In this region, in agreement with experimental observations, it is clear that the streaks and, for that matter, any definite organized structures are absent in the computed flow patterns.

In Fig. 19, one can distinguish several localized regions of very high-speed fluid (large concentration of solid lines) that are located on the high-speed streaks. Figure 21 shows the corresponding contour plot of pressure fluctuations, obtained at the same vertical location ($y^+ = 6.26$). It can be seen that, in contrast to $\overline{u}$, the pressure patterns are not elongated in the streamwise direction. However, the regions of high-pressure fluctuations are generally located in the vicinity of the "pockets" (see Falco, 1978) of high-speed fluid. This correspondence together with examination of the contour plots of $\overline{v}$ (see below) suggest that these pockets are "quasi-stagnation" regions which are formed as a result of the arrival of high-speed fluid to the wall layer. Moreover, the contour plots of normal and spanwise velocity fluctuations show that, like the pressure patterns, they do not exhibit elongated streaky structures. These observations imply that the wall layer may be viewed as a bed of low-speed fluid that is constantly subjected to the arrival of energetic eddies from the layers above. These energetic eddies (with the help of the strong mean shear) form the high-speed streaks in the wall region.

Figure 22 shows the contour plot of spanwise vorticity fluctuation,

$$\omega_z'' = \frac{\partial \overline{v}}{\partial x} - \frac{\partial \overline{u}''}{\partial y}$$

in the same x-z plane as in Fig. 19. Virtually all the regions with large vorticity fluctuations are associated with negative ω_z'' (large concentration of dashed lines). In these regions, the streamwise velocity profile has excess momentum with respect to the mean velocity (i.e., $\overline{u}'' > 0$). It should be pointed out that, in the vicinity of the wall, the relatively large positive values of $S(\overline{u}'')$ (Fig. 8) indicate that the existence of regions with $\overline{u}'' < 0$ are more probable than those with $\overline{u}'' > 0$. However, the structures with large magnitudes of $\overline{u}''$ are most likely associated with positive values of $\overline{u}''$. This is in agreement with the above observations.

Figures 23 and 24 show the $\overline{u}''$ and $\overline{v}$ patterns in an x-y plane (z = $4h_3$) which pass through the high-speed region in the lower left-hand corner of Fig. 19. In Fig. 24, a positive $\overline{v}$ (the solid lines) represents fluid moving in the positive y-direction, and a negative $\overline{v}$ (the dashed lines) represents fluid moving in the negative y-direction. It can be seen that, in the vicinity of the walls, the high-speed fluid elements $(\overline{u}'' \gg 0)$ correspond to the sweep event, i.e., $\overline{v} < 0$ near the lower wall, and $\overline{v} > 0$ near the upper wall. On the other hand, the low-speed fluid elements are generally being ejected from the wall regions. Clearly, both the sweep and ejection events have a positive contribution to the production of turbulent kinetic energy. One of the distinct features of Fig. 23 is that the high-speed structures near the walls are inclined at oblique angles with respect to the walls. This is the consequence of the action of mean shear on any fluid element from the outer layers that is moving toward the walls. Similar large-scale structures have been identified in the laboratory by Rajagopalan and Antonia

31

(1979). In their measurements, they report the mean angle of inclination of these structures to be 13°.

Figures 25 and 26 show the contour plots of $\overline{u''}$ and $\overline{v}$ in a y-z plane (x = 0). In these plots, only the lower half of the channel is shown. Throughout a significant portion of the region displayed, there is a negative correlation between $\overline{u''}$ and $\overline{v}$. Some of the regions where the correlation between $\overline{u''}$ and $\overline{v}$ is negative extend from the wall region to the channel centerline. In the wall region, the vertical and spanwise extent of the eddies is significantly smaller than in the regions away from the wall. In particular, near the wall in Fig. 24 the array of high- and low-speed fluid is clearly discernible.

Figure 27 shows the $\overline{u''}$, $\overline{v}$, and $\overline{w}$ patterns in the close vicinity of the wall ($y^+ < 46$, $y_w/\delta < 0.072$) in the same y-z plane as in Figs. 25 and 26. Here, the region near the wall is magnified, and hence the contour lines are highly distorted. In Fig. 27a, the mean spacing between two adjacent high-speed streaks (or low-speed ones) is about 250 in the wall units. The mean streak spacing can also be obtained from the $R_{11}(y_w = 0.025, r_3)$ profile in Fig. 7. In this figure, the negative peak occurs at $r_3^+ \approx 125$. This is the distance between two adjacent high- and low-speed streaks. Therefore, the corresponding distance between two high- (or low-) speed streaks is about 250 in the wall units. These two values are, surprisingly, in good agreement with each other but are considerably larger than the generally accepted value of $\lambda_{3m}^+ \simeq 100$. Therefore, as was pointed out in Sect. 3 for the Reynolds number considered in this study, the computational grid resolution is inadequate to resolve the streaks at their proper scale. However, as we have seen, the computed flow patterns, in the wall region, do exhibit the streaky structures at the finest scale permitted by the grid. The $R_{11}(y_w = 0.025, r_3)$ profile

from Case 1 in Table 1 shows that the mean streak spacing in that calculation is about 330 in the wall units. Thus, there is a definite improvement in the computed streak spacings with refinement of the computational grid resolution.

In Fig. 27b, one can see an array of positive and negative regions of v-contour lines that correspond to fluid moving away from and toward the wall. Intense shear layers are located at the interface between the energetic fluid streams moving toward and away from the wall. These shear layers may undergo Helmholtz-type instabilities in the y-z plane that result in the formation of streamwise vortices. These vortices can clearly be identified in Fig. 28, where the contour plot of ω_x in the same y-z plane is shown.

Comparison of Figs. 27b and 27c demonstrates that, in the close vicinity of the wall $(y^+ < 10)$, the high-speed vertical streams with negative normal component of velocity produce a flow pattern similar to that of a jet impingement on a plate. On the other hand, the high-speed vertical streams with positive normal component of velocity are formed from two streams with opposite velocities in the spanwise direction. Since the high-speed fluid elements arriving at the wall region are more energetic than the viscous-dominated fluid moving away from the wall, there is a net transfer of energy from the normal component of turbulence intensity to the horizontal components (the splatting effect). This appears to be the reason for the behavior of the pressure-strain correlations in the vicinity of the wall (Fig. 11). In addition, it should be noted that the impingement of fluid from outer layers on the wall leads to stretching of spanwise vorticity fluctuations (as well as streamwise vorticity) which can be an important mechanism for its amplification.

Near the wall, in Fig. 27c, one can see large gradients of the spanwise velocity component in the normal direction. On the other hand, due to the

wall-suppression effect, the vertical component of turbulence intensity is degraded there. Large values of $\partial w/\partial y$ lead to high values of streamwise vorticity fluctuations in the neighborhood of the wall. In Fig. 28, it can be seen that the regions with large ω_x are concentrated near the wall. Here, two distinct areas can be identified: the first is slightly above the wall $(10 < y^+ < 40)$, where the large amplitudes of ω_x are due to revolving fluid elements induced by the intense shear layers shown in Fig. 27b; the second is in the immediate neighborhood of the wall $(y^+ < 10)$, where the splatting effect and no-slip boundary conditions lead to large values of $\partial w/\partial y$ and consequently ω_x. In Fig. 9, the profile of $< \omega_x^2 >^{1/2}$ attained its maximum at the wall and displayed a local maximum at $y^+ \simeq 30$. The maximum at the wall is a result of the splatting effect, and the local maximum is located in the first region described above.

So far, we have examined the eddy structure of the turbulent channel flow by considering two-dimensional contour plots of instantaneous velocity, pressure, and vorticity field. To gain a better insight into the unsteady dynamics of the flow, a computer motion picture simulating flow-visualization experiments with hydrogen-bubble wires was made. Several sequences of film were generated. At regular intervals in each sequence $(\Delta \tau = 0.015$ in non-dimensional time units), 128 particles were generated along a line either parallel or normal to the walls. These particles were followed until the memory capacity of the graphic display unit was depleted. Here, we briefly discuss some of the still photographs taken from the film.

Figure 29 shows the particles generated along a line parallel to the z-axis ("z-wire") and located near the lower wall $(y^+ = 12)$. In this figure, the wall-layer streaks are clearly evident. On several occasions when viewing the motion picture, it was observed that the particles generated near the wall were violently ejected to regions as far away from the wall as $y^+ \simeq 400$.

Figure 30 shows the time history of the particles generated along a "z-wire" which is located distant from the wall $(y^+ = 319)$. It can be seen that the coherent streaky structures that are the characteristic of wall layer turbulence are absent in the regions away from the walls.

In Fig. 31, the time history of the particles generated along a line normal to the walls is shown. The formation of inflexional velocity profiles and strong shear layers near the walls is very similar to the corresponding photographs obtained by Kim et al. (1971) in their flow-visualization studies. This resemblance is even more pronounced in Fig. 32, where 128 particles were generated along the same vertical line, as in Fig. 31, but extended from the lower wall to $y = -0.5$. Here, one can see several profiles with multiple inflexion points. In addition, in this figure, the formation of a streamwise vortex with an axis of rotation which is tilted outward in the flow direction and its ultimate breakup are clearly discernible.

8. Summary and Conclusions

In this study, turbulent plane Poiseuille flow has been numerically simulated at a moderate Reynolds number. Most of the calculations were carried out with 516,096 grid points on the ILLIAC IV comuter. The agreement of the computed mean velocity profile and turbulence statistics with experimental data is good.

The resolvable portion of the statistical correlations appearing in the Reynolds stress equations was calculated. The role and relative importance of the various terms in these equations were discussed.

The structure of the flow field was examined in some detail. It was found that, in agreement with experimental observations, the computed flow pattern in the wall region was characterized by coherent structures of low- and high-speed streaks alternating in the spanwise direction. In this region,

35

the large-amplitude, streamwise velocity fluctuations were primarily due to the arrival of high-speed fluid elements from adjacent layers. The regions with large-amplitude, streamwise vorticity, ω_x, were concentrated near the wall. Slightly above the wall, these regions contained revolving fluid elements induced by strong shear layers in the cross-stream plane. In the immediate neighborhood of the wall, the splatting effect led to large magnitudes of ω_x and instigated transfer of energy from the normal component of turbulent kinetic energy to the horizontal components.

With three-dimensional, time-dependent, numerical simulation of turbulence, one is capable of obtaining detailed, instantaneous information about the flow at thousands of spatial locations. This information can effectively be used to study the structure and statistical properties of the flow and their relation to each other. Furthermore, with the aid of computer graphics and the ability to move back in time and recreate an event in the flow after it has already been observed, one has the unique opportunity to study the mechanics of turbulent shear flows. Thus, with the anticipated advances in computer technology, it is expected that in the near future numerical simulation of turbulent flows will make important contributions to turbulence research.

Case	N_1	N_3	L_1/δ	L_3/δ	h_1^+	h_3^+	h_1/δ	h_3/δ	Integration Time[†]	Average Time[†]
1	64	64	4π	$\frac{2}{3}\pi$	125.7	20.9	0.196	0.033	4.0	1.6
2	64	128	4π	π	125.7	15.7	0.196	0.025	3.65	0.75
3	64	128	3π	π	94.2	15.7	0.147	0.025	3.9	1.6
4	64	128	2π	π	62.8	15.7	0.098	0.025	4.6	2.3

[†]In δ/u_τ units.

Table 1. Specifications of the computed cases

References

Batchelor, G. K. (1953), The Theory of Homogeneous Turbulence, Cambridge, The University Press.

Brodkey, R. S., Wallace, J. M., and Eckelmann, H. (1974), "Some Properties of Truncated Turbulence Signals in Bounded Shear Flows," J. Fluid Mech., 63, 209.

Chapman, D. R. (1979), "Computational Aerodynamics Development and Outlook," AIAA J., 17 (12), 1293-1313.

Clark, J. A. (1968), "A Study of Incompressible Turbulent Boundary Layers in Channel Flow," J. Basic Engrg., 90, 455.

Clark, J. A., and Markland, E. (1970), "Vortex Structures in Turbulent Boundary Layers," Aeronaut. J., 74, 243.

Comte-Bellot, G. (1963), "Contribution a l'etude de la Turbulence de Conduite," doctoral thesis, University of Grenoble.

Corcos, G. M. (1962), Univ. of Calif., Inst. of Engrg. Res. Report, Series 183, No. 1; from Willmarth and Wooldridge (1962).

Daly, J., and Harlow, F. H. (1970), "Transport Equations in Turbulence," Phys. of Fluids, 13 (11), Nov. 1970, 2634-2649.

Deardorff, J. W. (1970), "A Numerical Study of Three-Dimensional Turbulent Channel Flow at Large Reynolds Numbers," J. Fluid Mech., 41, 453-480.

Falco, R. E. (1978), "The Role of Outer Flow Coherent Motions in the Production of Turbulence Near a Wall," in Coherent Structures of Turbulent Boundary Layers (C. R. Smith and D. E. Abbott, eds.), AFOSR/Lehigh, 1978.

Grötzbach, G., and Schumann, U. (1977), "Direct Numerical Simulation of Turbulent Velocity-, Pressure-, and Temperature-Fields in Channel Flows," Symposium on Turbulent Shear Flows, April 18-20, 1977, Penn. State Univ.

Harlow, F. H., and Welch, J. E. (1965), "Numerical Calculation of Time-Dependent Viscous Incompressible Flow," Phys. Fluids, 8, 2182.

Hinze, J. O. (1975), Turbulence, McGraw-Hill, Inc., 2nd ed.

Hussain, A.K.M.F., and Reynolds, W. C. (1975), "Measurements in Fully Developed Turbulent Channel Flow," J. Fluids Engrg., 97, 568-578.

Kim, H. T., Kline, S. J., and Reynolds, W. C. (1971), "The Production of Turbulence Near a Smooth Wall in a Turbulent Boundary Layer," J. Fluid Mech., 50, 133.

Kim, J., and Moin, P. (1979), "Large Eddy Simulation of Turbulent Channel Flow--ILLIAC IV Calculation," AGARD Conference Proceedings, No. 271, Turbulent Boundary Layers--Experiments, Theory, and Modeling, The Hague, Netherlands, Sept. 24-26, 1979.

Kline, S. J., Reynolds, W. C., Schraub, F. A., and Runstadler, P. W. (1967), "The Structure of Turbulent Boundary Layers," J. Fluid Mech., 30, 741.

Kreplin, H., and Eckelmann, H. (1979), "Behavior of the Three Fluctuating Velocity Components in the Wall Region of a Turbulent Channel Flow," Phys. Fluids, 22 (7), July, 1979, 1233-1239.

Kwak, D., Reynolds, W. C., and Ferziger, J. H. (1975), "Three-Dimensional Time-Dependent Computation of Turbulent Flows, Report No. TF-5, Dept. of Mech. Engrg., Stanford University.

Laufer, J. (1954), "The Structure of Turbulence in Fully Developed Pipe Flow," NACA Report 1174.

Leonard, A. (1974), "On the Energy Cascade in Large-Eddy Simulations of Turbulent Fluid flows," Adv. in Geophysics, 18A, 237.

Mansour, N. N., Moin, P., Reynolds, W. C., and Ferziger, J. H. (1977), "Improved Methods for Large Eddy Simulation of Turbulence," Proc. Symp. on Turbulent Shear Flows, Penn. State Univ.

Merriam, M. (1978), private communication.

Moin, P., Reynolds, W, C., and Ferziger, J. H. (1978), "Large Eddy Simulation of Incompressible Turbulent Channel Flow," Report No. TF-12, Dept. of Mech. Engrg., Stanford University.

Moin, P., and Kim, J. (1980), "On the Numerical Solution of Time-Dependent, Viscous, Incompressible Fluid Flows Involving Solid Boundaries," J. Comp. Physics, 35, May, 1980, 381-392.

Orszag, S. A. (1972), "Comparison of Pseudospectral and Spectral Approximation," Studies in Appl. Math., LI, No. 3, Sept. 1972, 253.

Rajagopalan, S., and Antonia, R. A. (1979), "Some Properties of the Large Structure in a Fully Developed Turbulent Duct Flow, Phys. Fluids, 22, 1979, 614.

Runstadler, P. W., Kline, S. J., and Reynolds, W. C. (1963), "An Investigation of the Flow Structure of the Turbulent Boundary Layer," Report No. MD-8, Dept. of Mech. Engrg., Stanford University.

Sabot, J., and Comte-Bellot, G. (1976), "Intermittency of Coherent Structures in the Core Region of Fully Developed Turbulent Pipe Flow," J. Fluid Mech., 74, 1976, 767.

Schumann, U. (1973), "Ein Verfahren zur direckten numerischen turbulenter Strömungen in Platten und Ringspaltkanälen und über seine Anwendung zur Untersuchung von Turbulenzmodellen," Universität Karlsruhe (NASA Tech. Translation, NASA TTF 15,391).

Schumann, U. (1975), "Subgrid Scale Model for Finite Difference Simulations of Turbulent Flows in Plane Channels and Annuli," J. Comp. Phys., 18, 376-404.

Schumann, U., Grötzbach, G., and Kleiser, L. (1979), "Direct Numerical Simulation of Turbulence," PSB-Bericht 680 (Kl. I), Kernforschungszentrum Karlsruhe.

Shaanan, S., Ferziger, J. H., and Reynolds, W. C. (1975), "Numerical Simulation of Turbulence in the Presence of Shear," Report No. TF-6, Dept. of Mech. Engrg., Stanford University.

Townsend, A. A. (1956), The Structure of Turbulent Shear Flow, Cambridge, the University Press, 1956.

Van Driest, E. R. (1956), "On Turbulent Flow Near a Wall," J. Aeronaut. Sci., 23, 1956, 1007.

Willmarth, W. W., and Wooldridge, C. E. (1962), "Measurement of the Fluctuating Pressure at the Wall beneath a Thick Turbulent Boundary Layer," J. Fluid Mech., 14, corrigendum: J. Fluid Mech., 21 (1965).

Willmarth, W. W. (1975), "Pressure Fluctuations beneath Turbulent Boundary Layers," Annual Rev. of Fluid Mech., 1975.
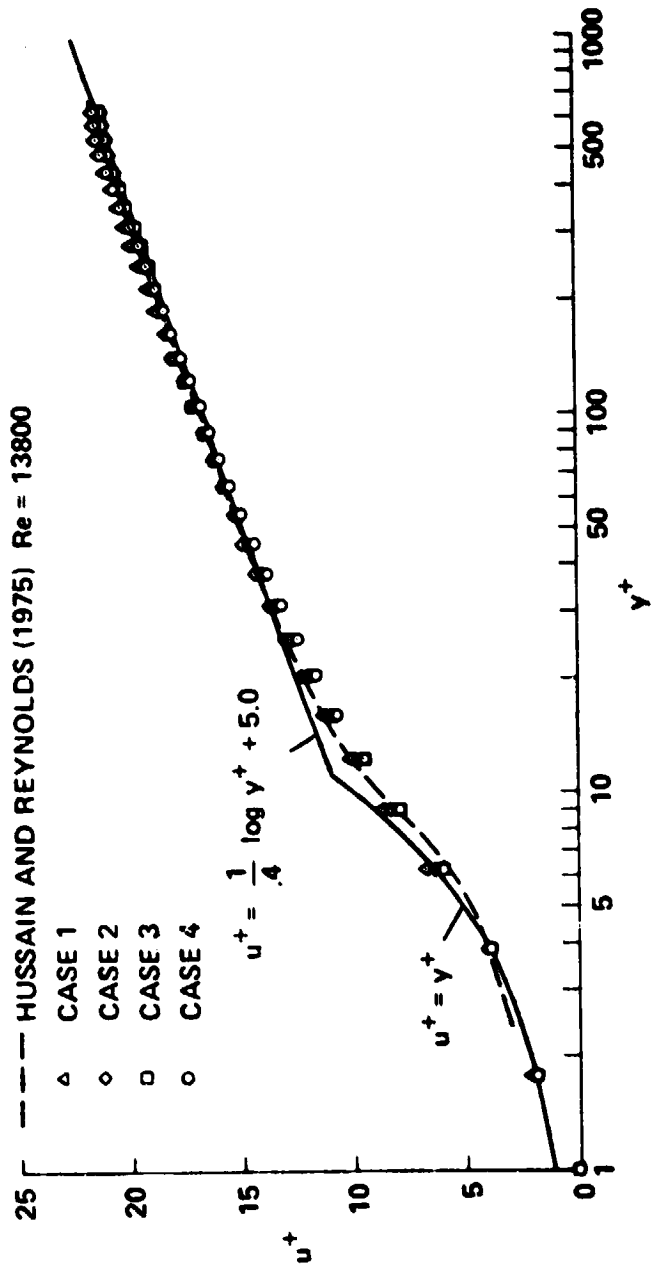
Fig. 1. Mean velocity profiles from four computed cases and comparison with experimental data.
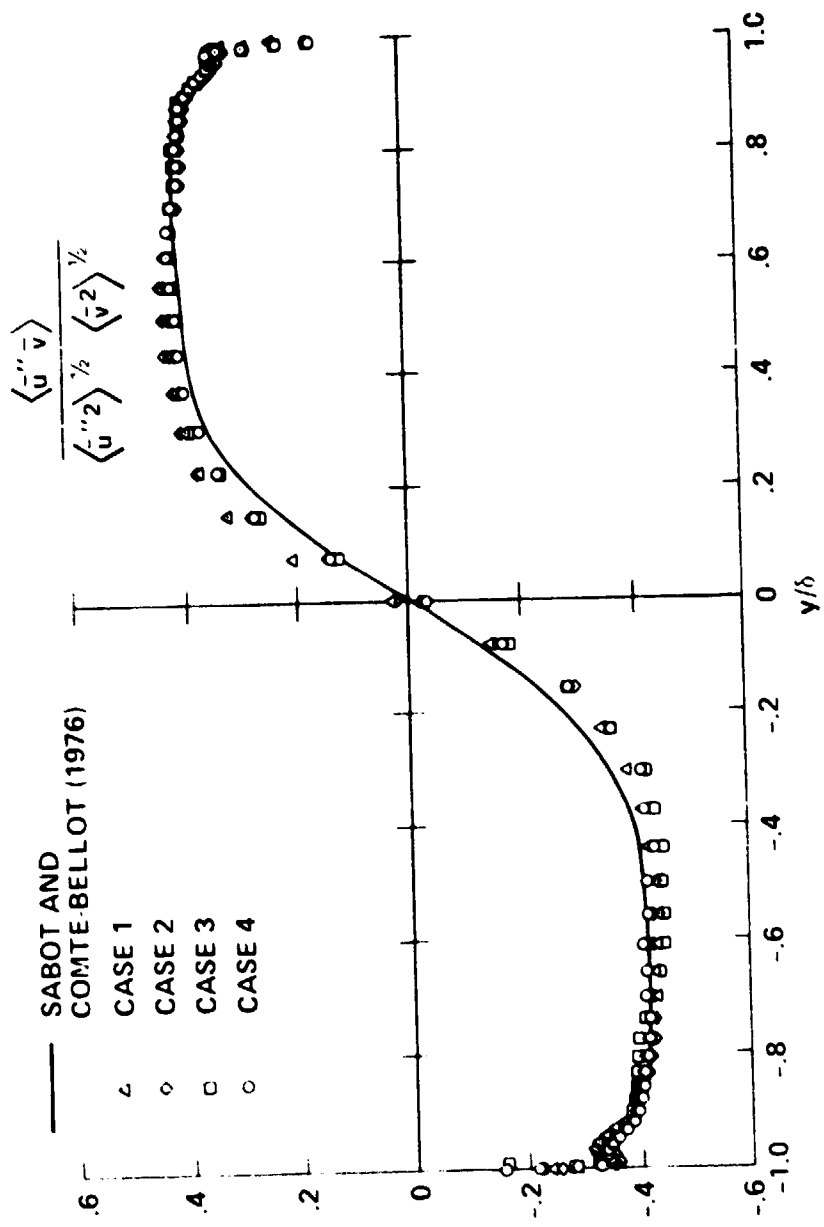
Fig. 2. Correlation coefficients between $\overline{u''}$ and $\overline{v}$ from four computational cases and comparison with experimental data.
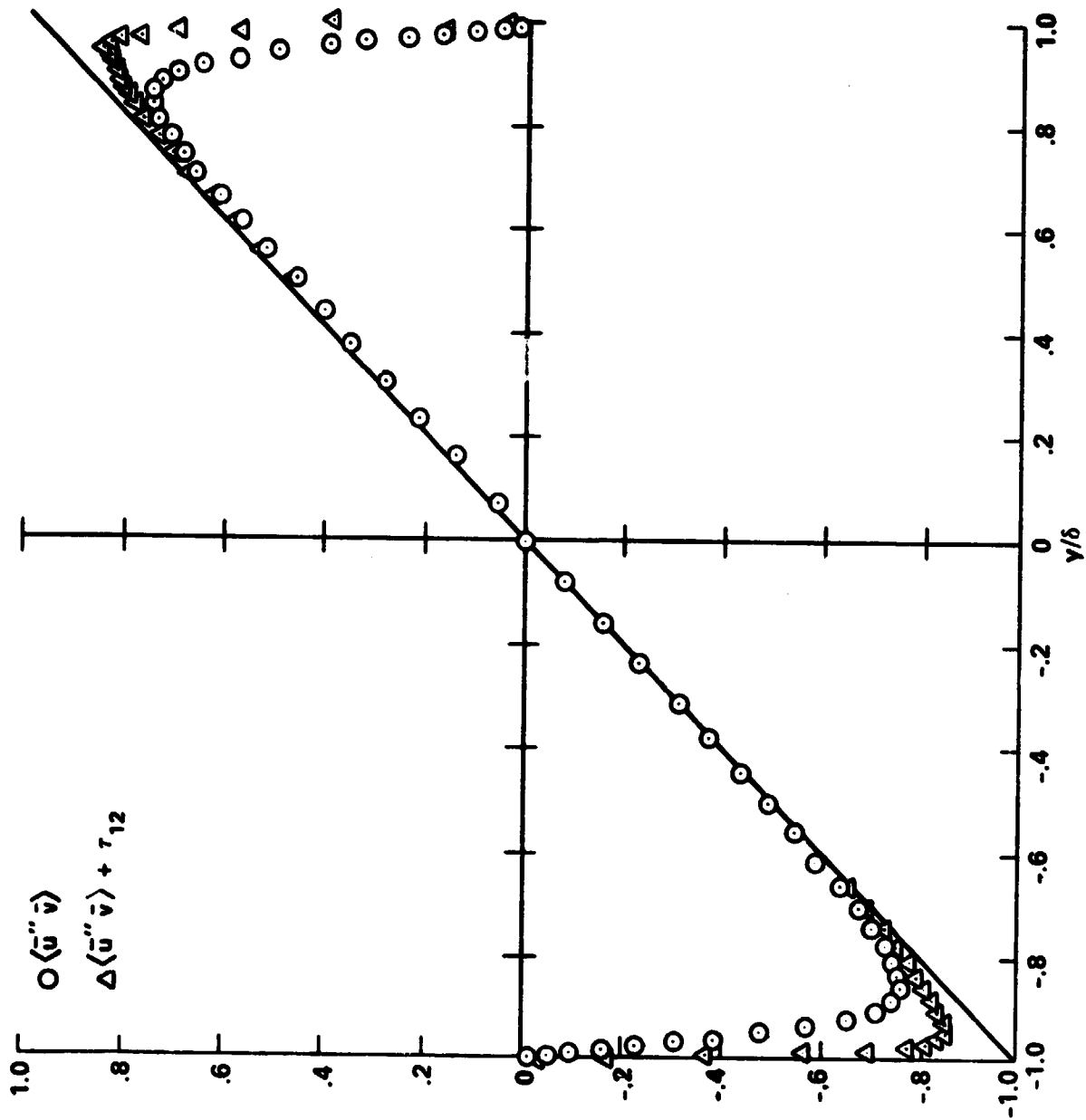
Fig. 3. Resolvable and total turbulence shear stress.

43
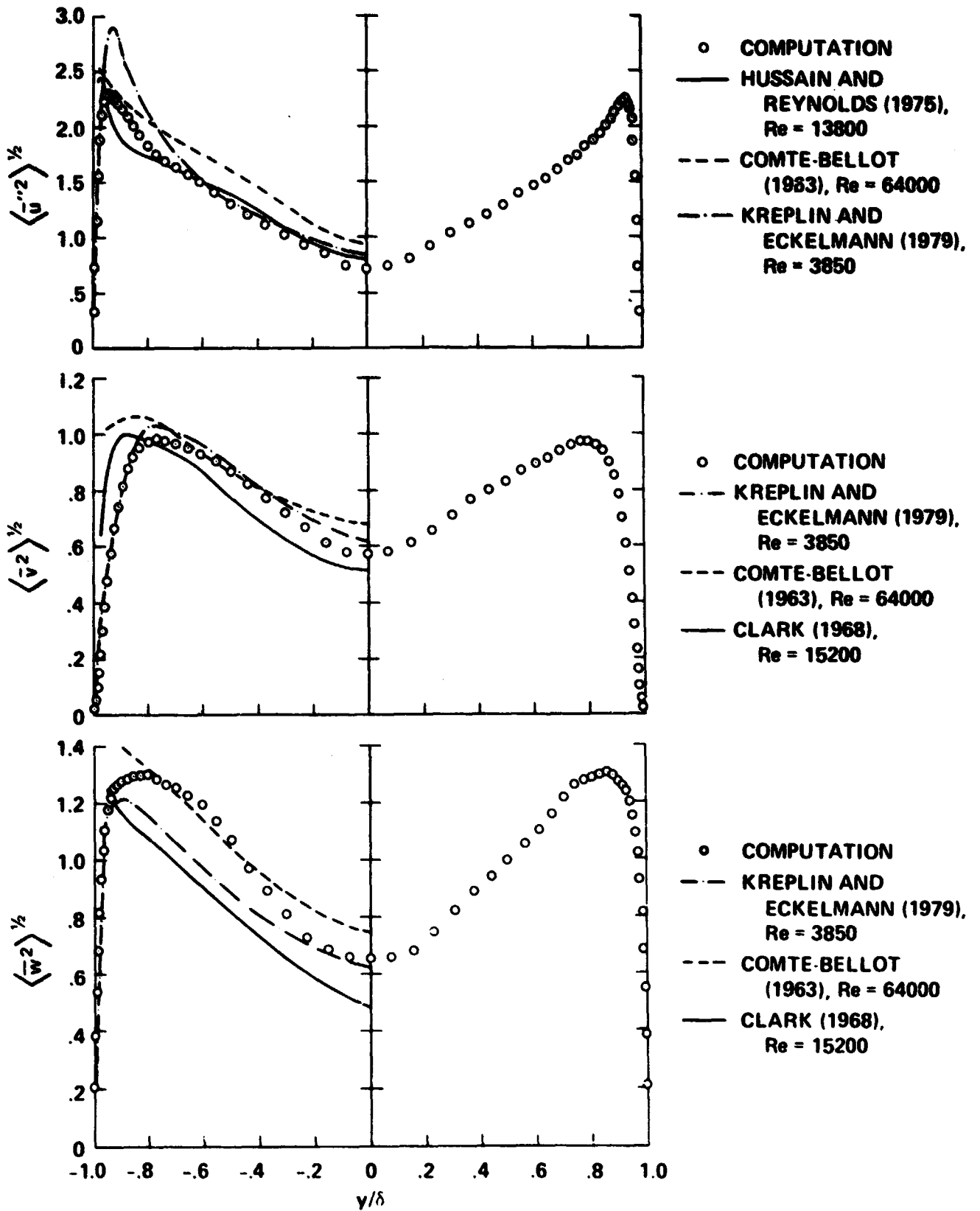
Fig. 4. Resolvable turbulence intensities and comparison with experimental data.
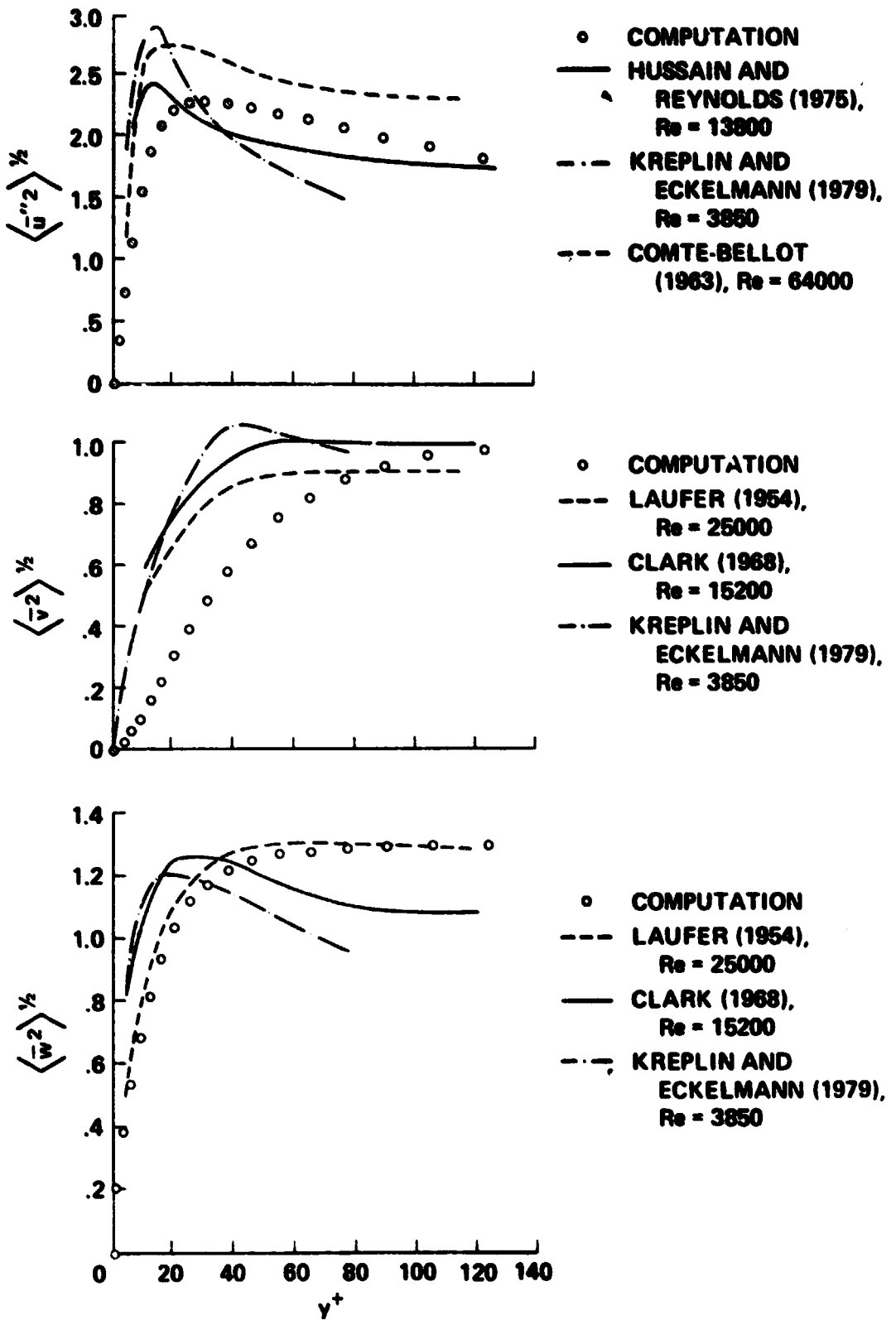
Fig. 5. Resolvable turbulence intensities in the vicinity of the lower wall and comparison with experimental data.
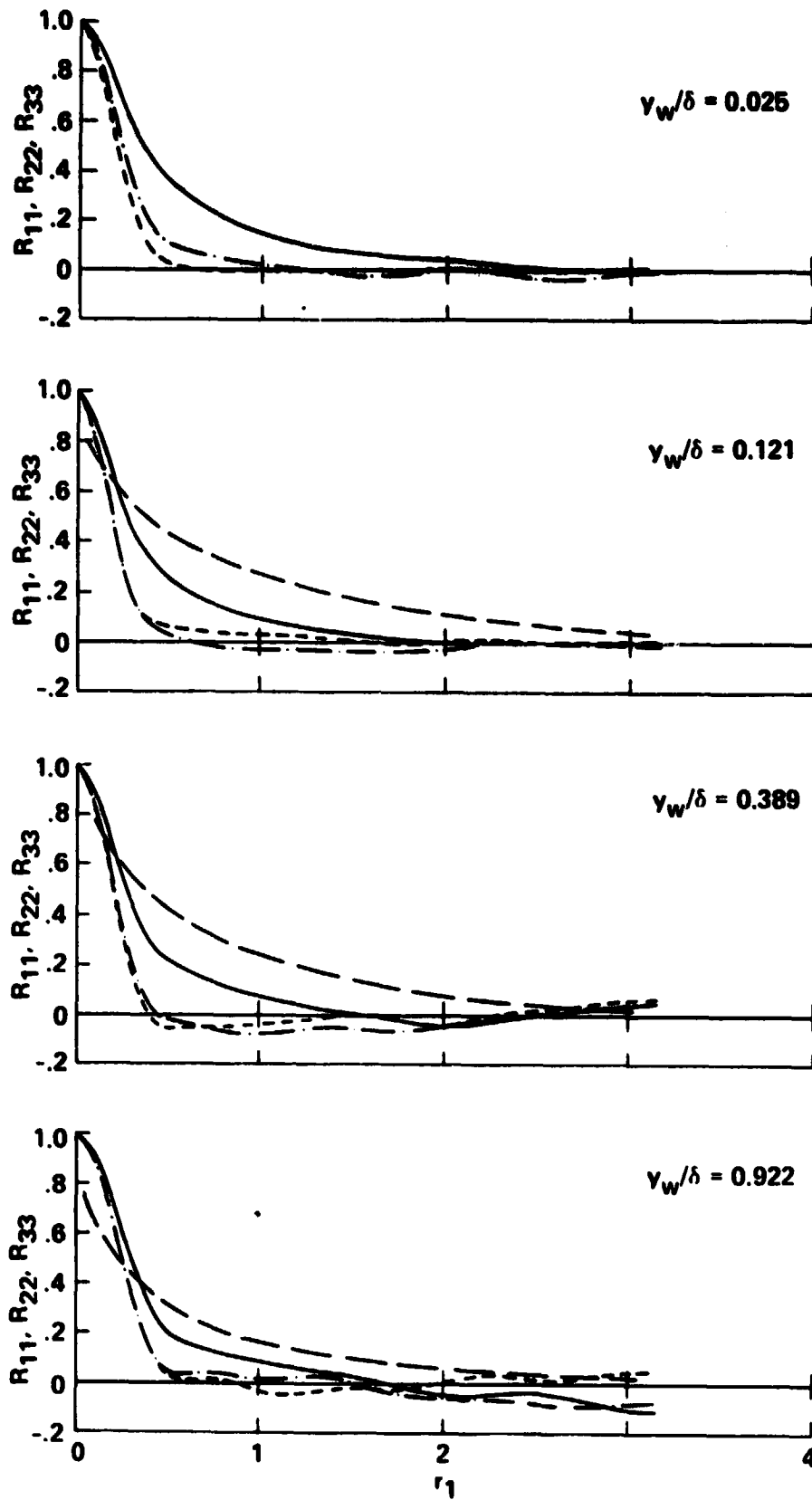
Fig. 6. Streamwise two-point correlation function. ——, R_{11}; - - - - . R_{22}; —— . ——, R_{33}; —— —— —, R_{11}, Comte-Bellot (1965).
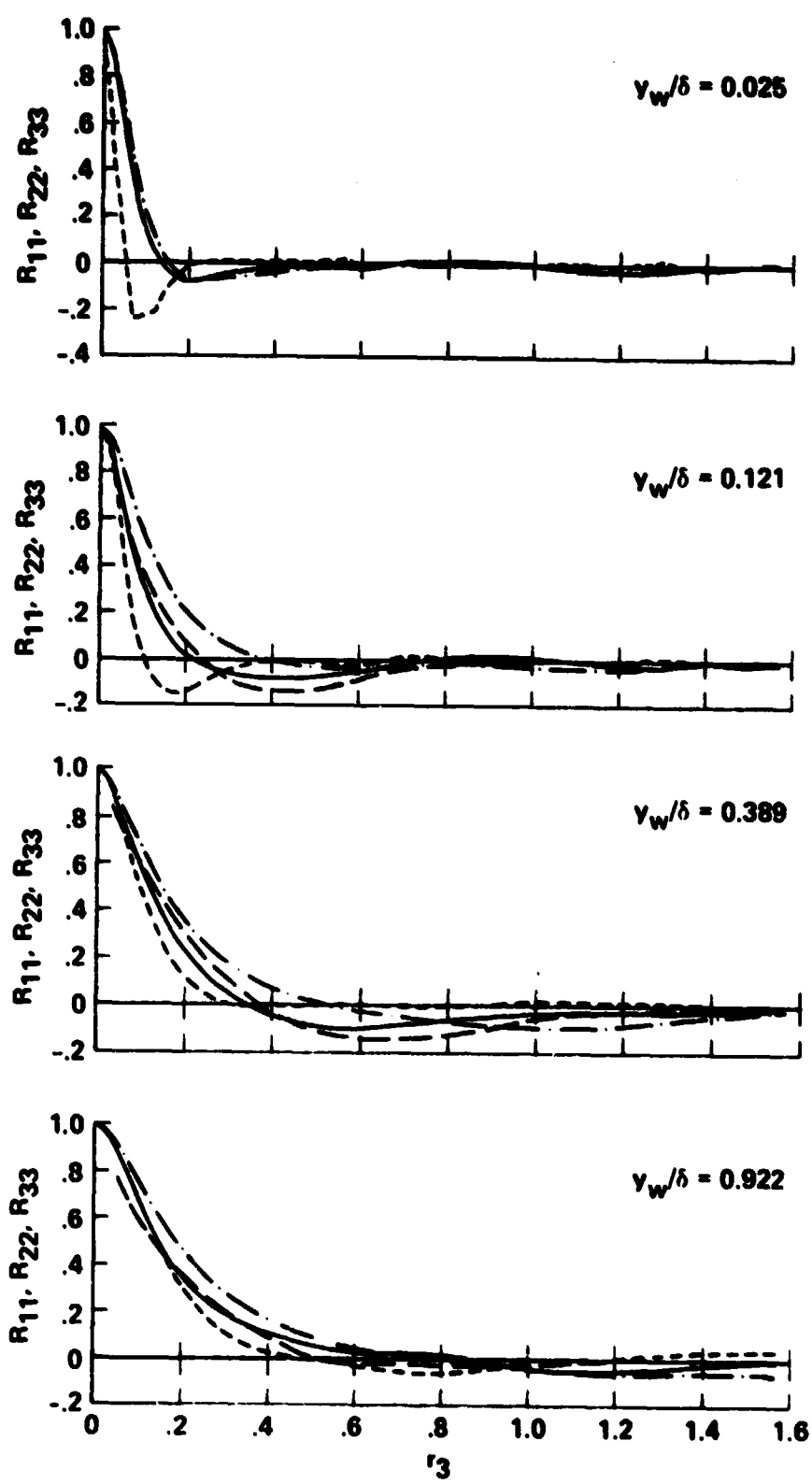
Fig. 7. Spanwise two-point correlation function. ———, R_{11}; – – – –, R_{22}; ——— · ———, R_{33}; — — — —, R_{11}, Comte-Bellot (1963).
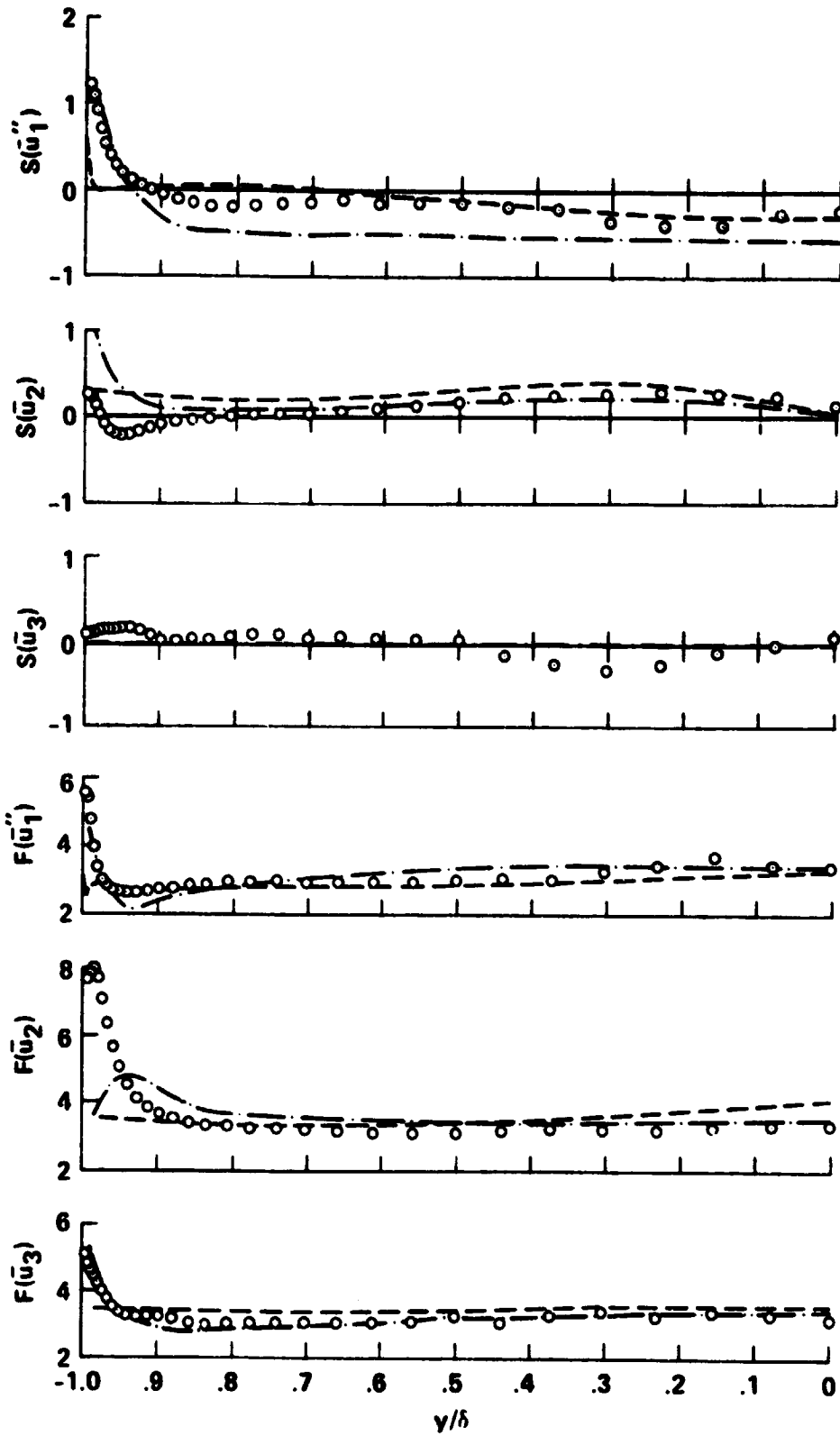
Fig. 8. Skewness and flatness factors. ⊙ , computation; —— • —— , Kreplin and Eckelmann (1979); — — — —, Comte-Bellot (1963).
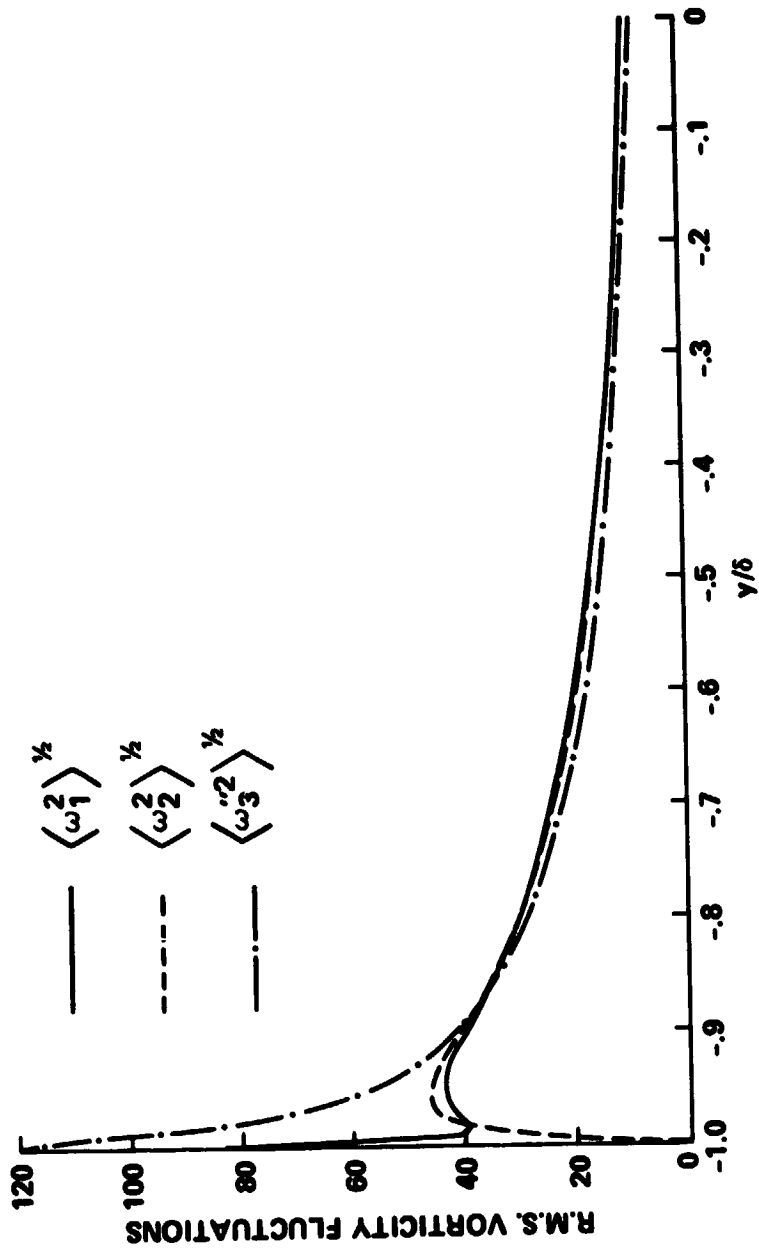
Fig. 9. Resolvable root-mean square vorticity fluctuations.
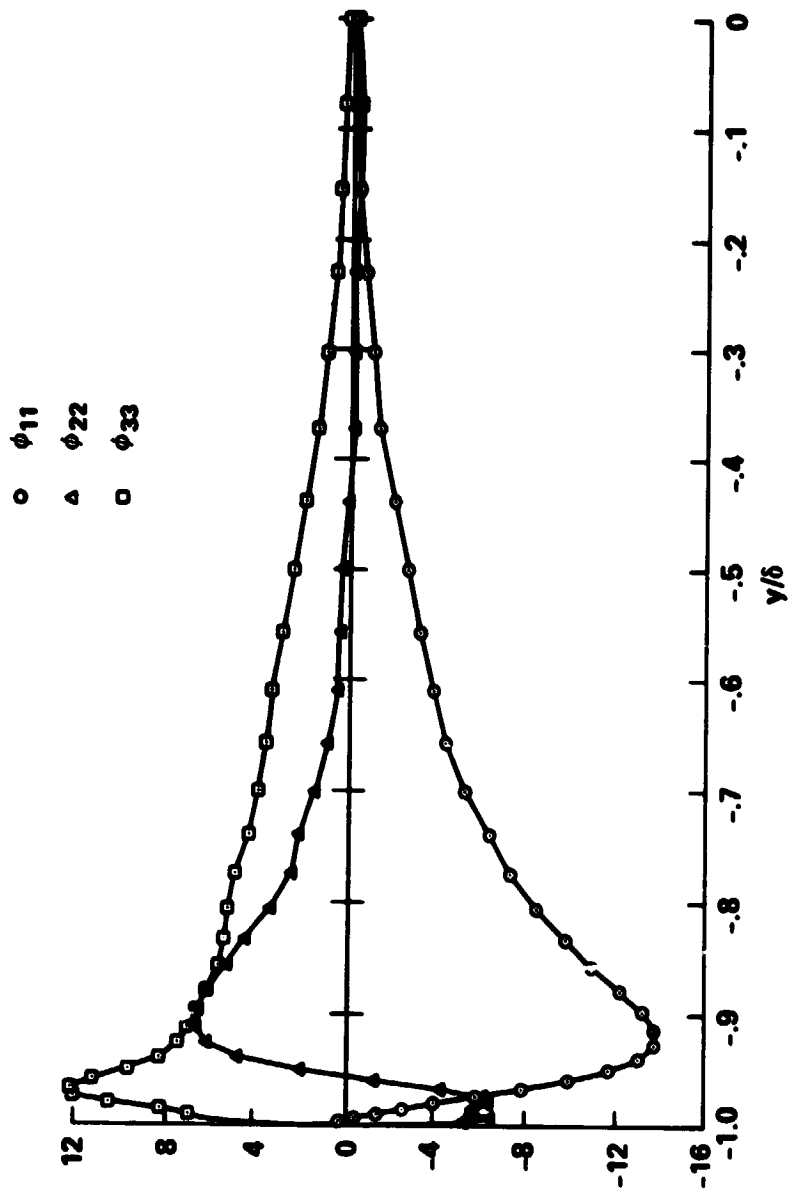
Fig. 10. Resolvable portion of the trace of the pressure-strain correlation tensor.
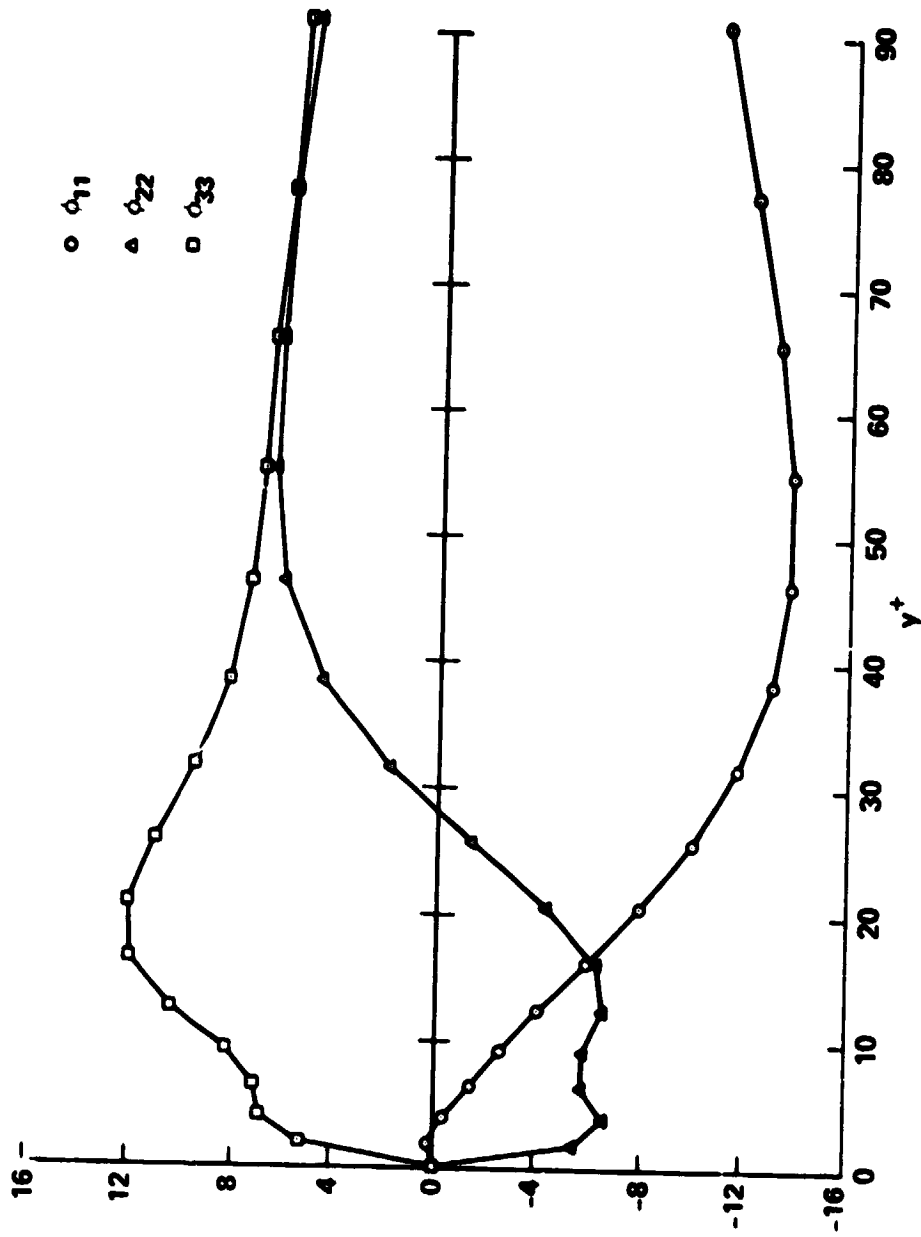
Fig. 11. Resolvable portion of the trace of the pressure-strain correlation
tensor in the vicinity of the lower wall.
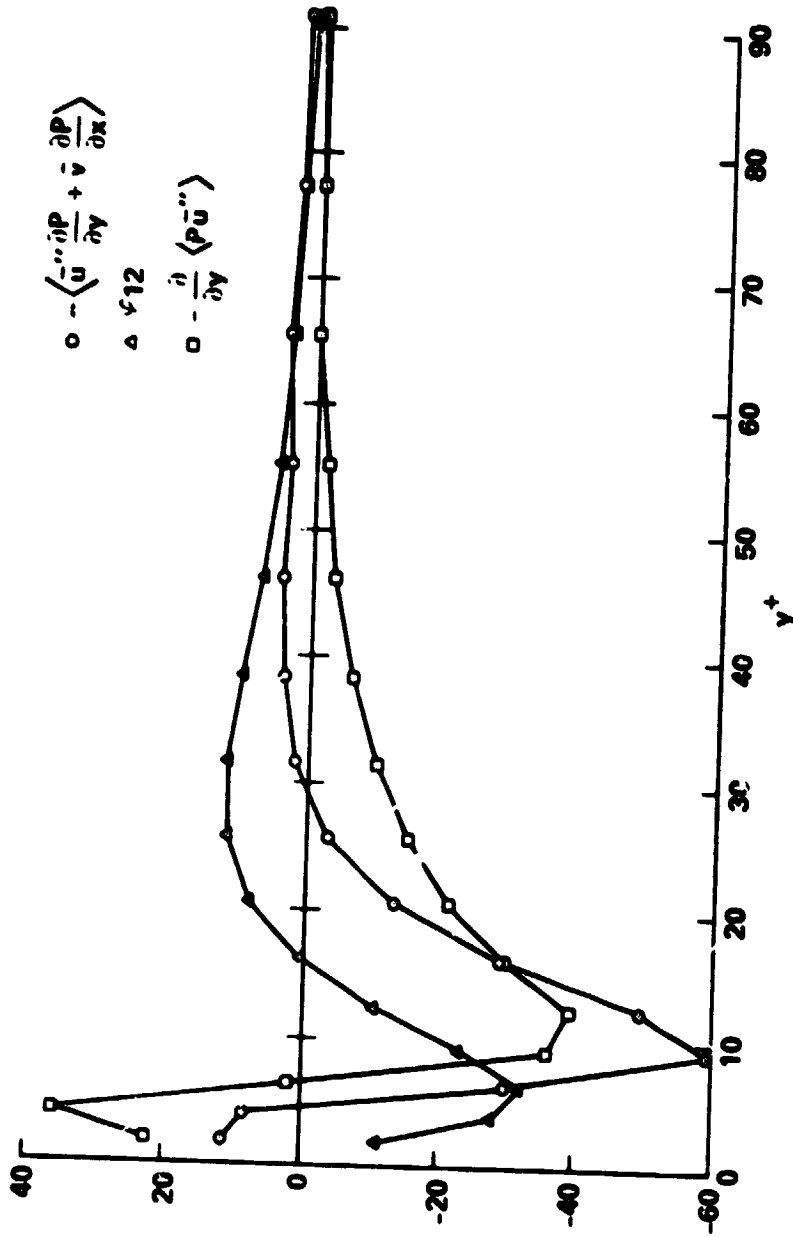
Fig. 12. Resolvable portion of the off-diagonal element of the pressure-strain correlation tensor, ϕ_{12}, pressure diffusion term, $-\frac{\partial}{\partial y}\langle\overline{P u''}\rangle$, and their sum, $P_{uv} = -\langle \overline{u''}\frac{\partial P}{\partial y} + \overline{v}\frac{\partial P}{\partial x}\rangle$.
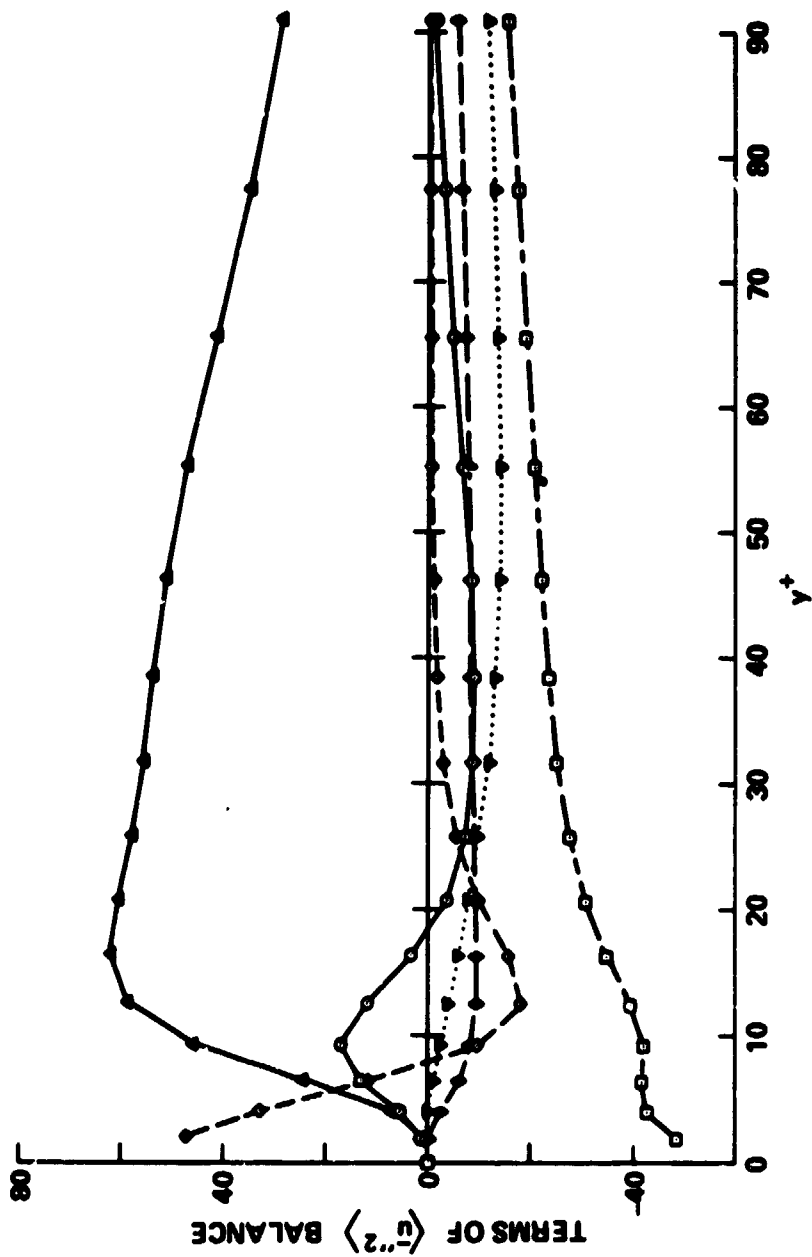
Fig. 13. Balance of the resolvable portion of the streamwise component of turbulent kinetic energy △ , production; ⊙ , convection; ◈ : cascade; ▽ , velocity-pressure gradient; ▢ , dissipation; ◇ : viscous diffusion.

53
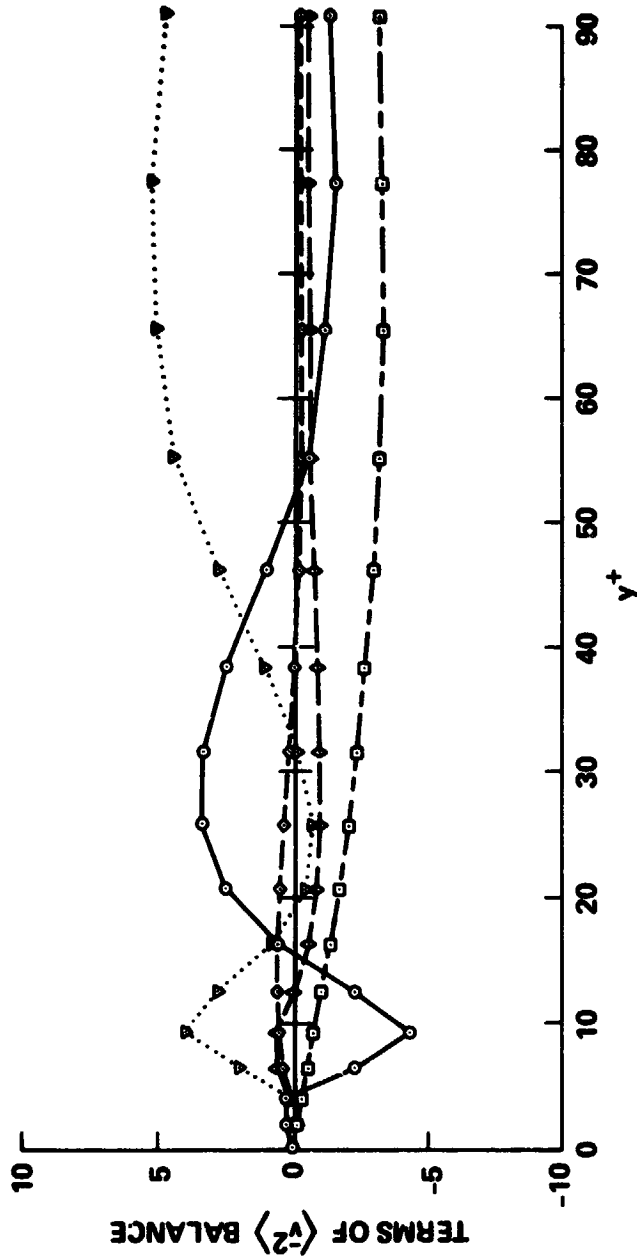
Fig. 14. Balance of the resolvable portion of normal component of turbulent kinetic energy. See caption of Fig. 13 for details.
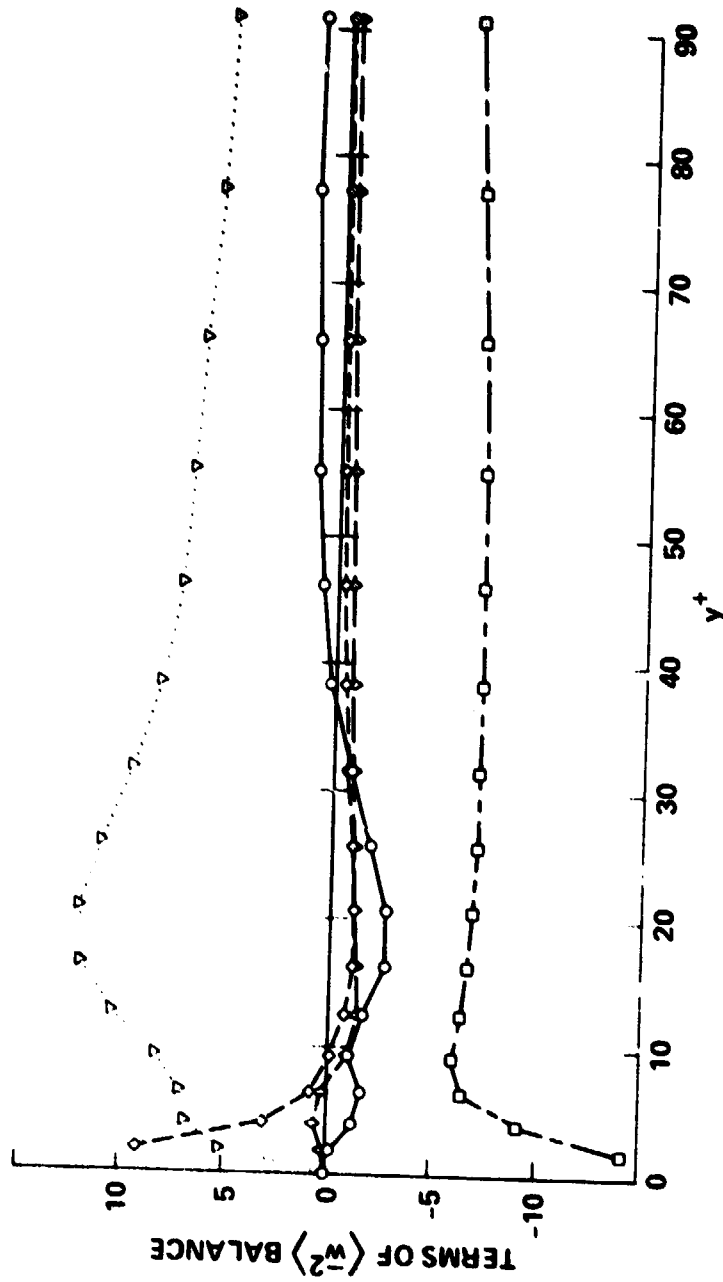
Fig. 15. Balance of the resolvable portion of spanwise component of turbulent kinetic energy. See caption of Fig. 13 for details.
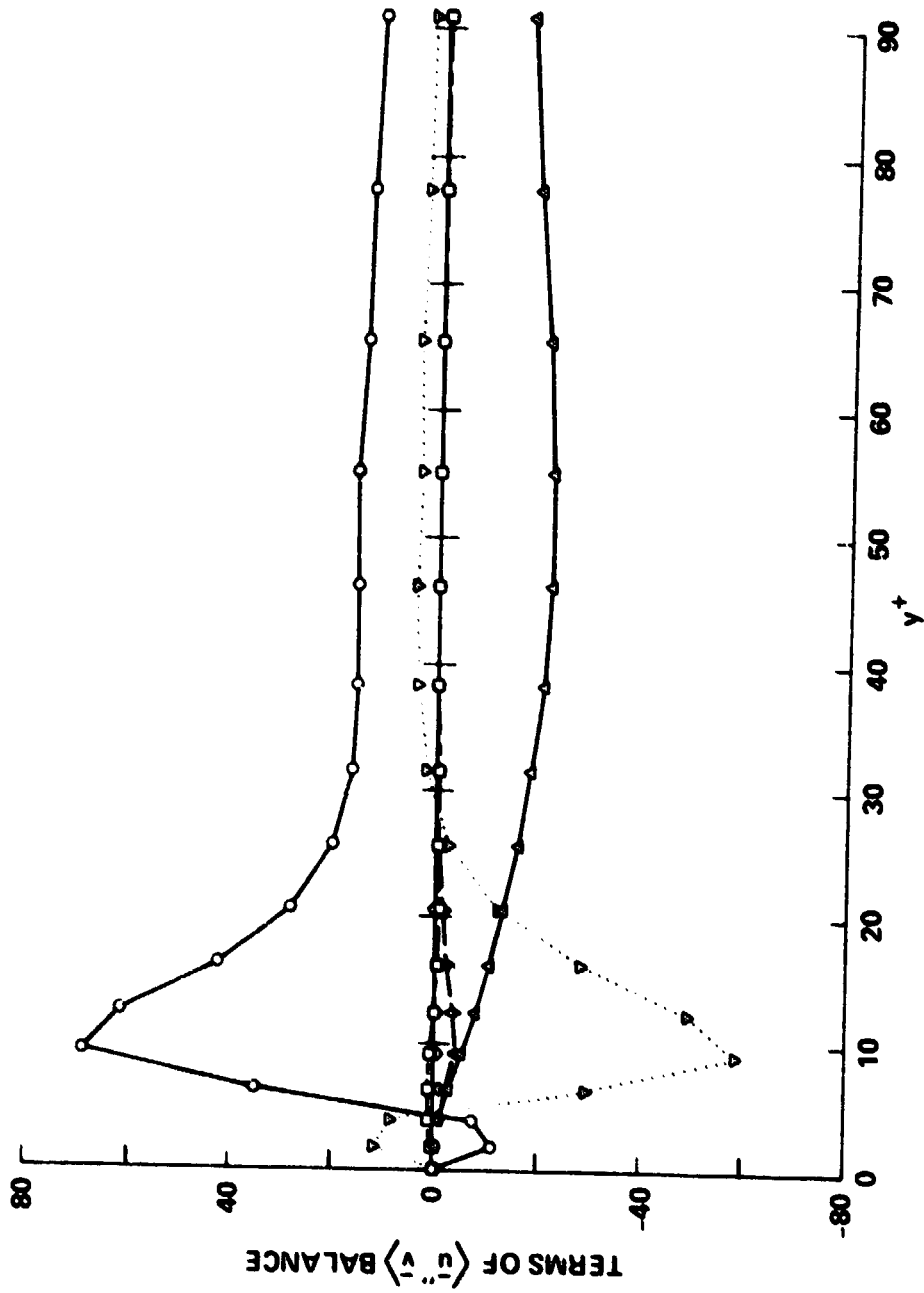
Fig. 16. Balance of the resolvable portion of turbulence shear stress. See caption of Fig. 13 for details.
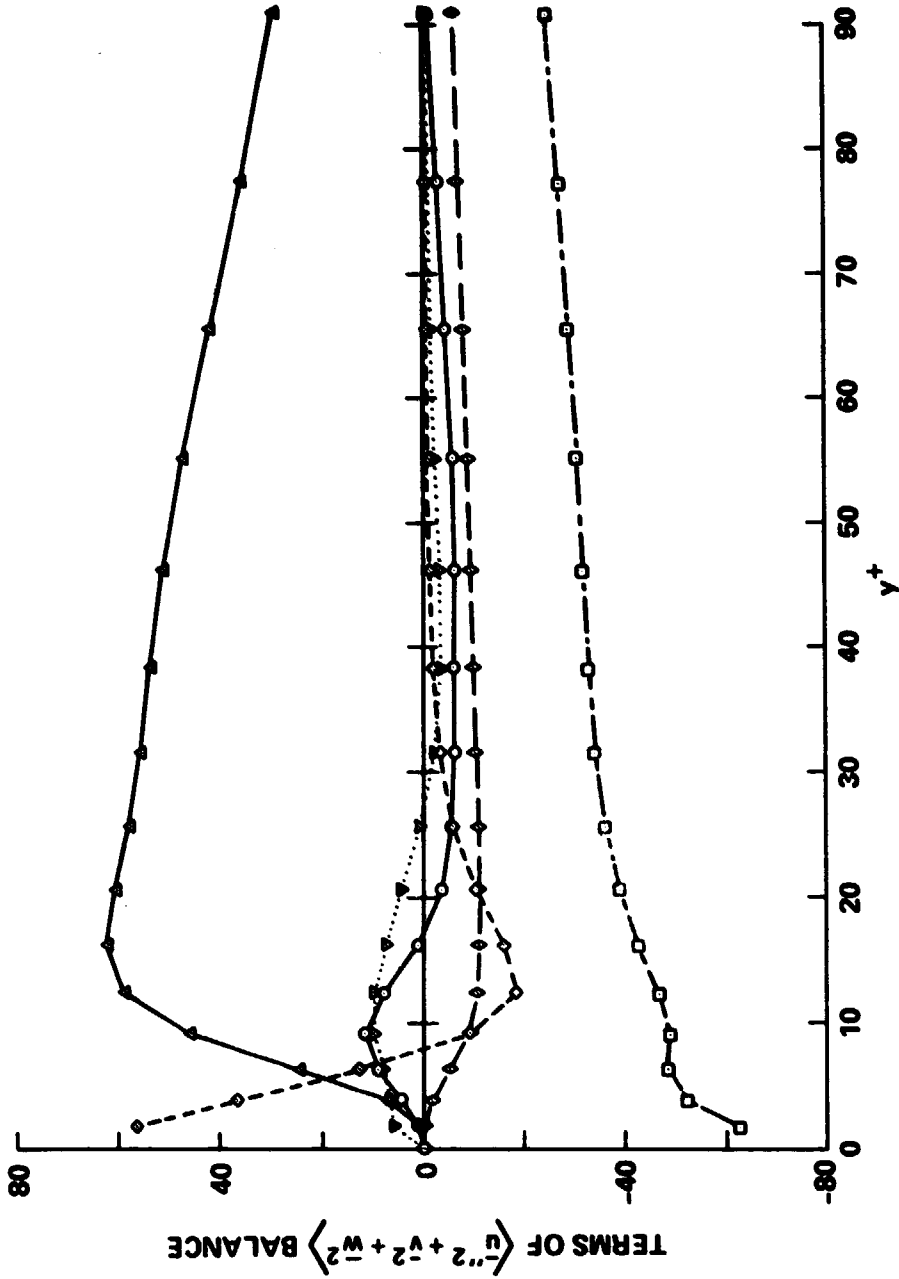
Fig. 17. Balance of the resolvable turbulence kinetic energy. See caption of Fig. 13 for details.
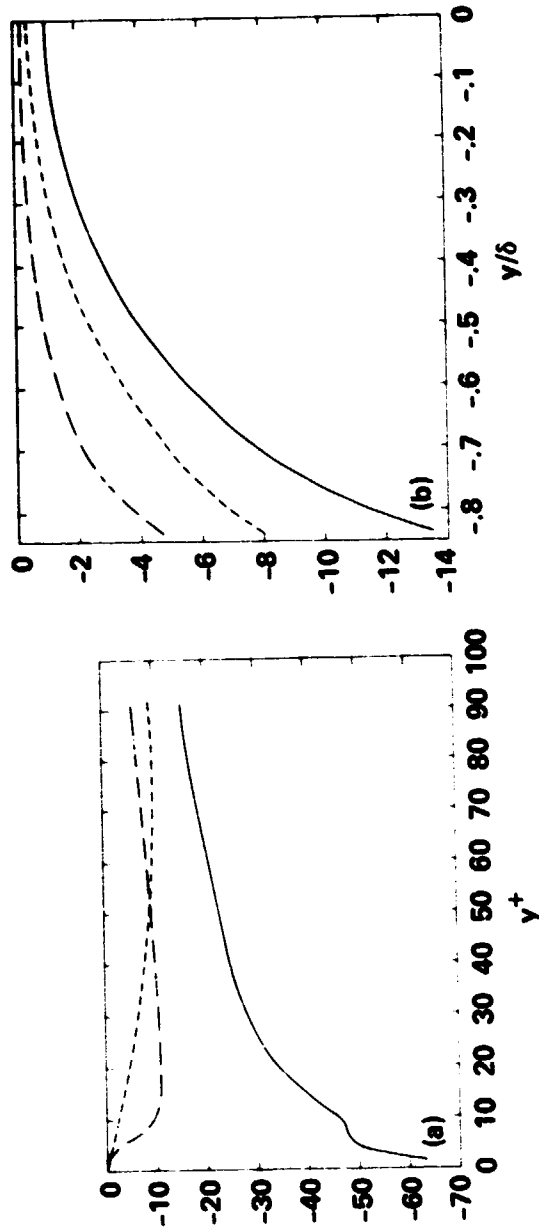
Fig. 18. Dissipation of turbulent kinetic energy due to molecular and eddy viscosities and the cascade term in the vicinity of the lower wall (a) and in the regions away from the wall (b):

$$\underline{\hspace{2cm}} \;,\; -\frac{2}{Re}<\frac{\partial \bar{u}_i''}{\partial x_j}\frac{\partial \bar{u}_i''}{\partial x_j}>\;;\; \text{-----}\;,\; -2<\nu_T\frac{\partial \bar{u}_i''}{\partial x_j}\frac{\partial \bar{u}_i''}{\partial x_j}>\;;$$

$$\underline{\cdot\underline{\hspace{1.5cm}}} \;,\; -2<\bar{u}_i''\frac{\partial}{\partial x_j}\lambda_{ij}>\;.$$
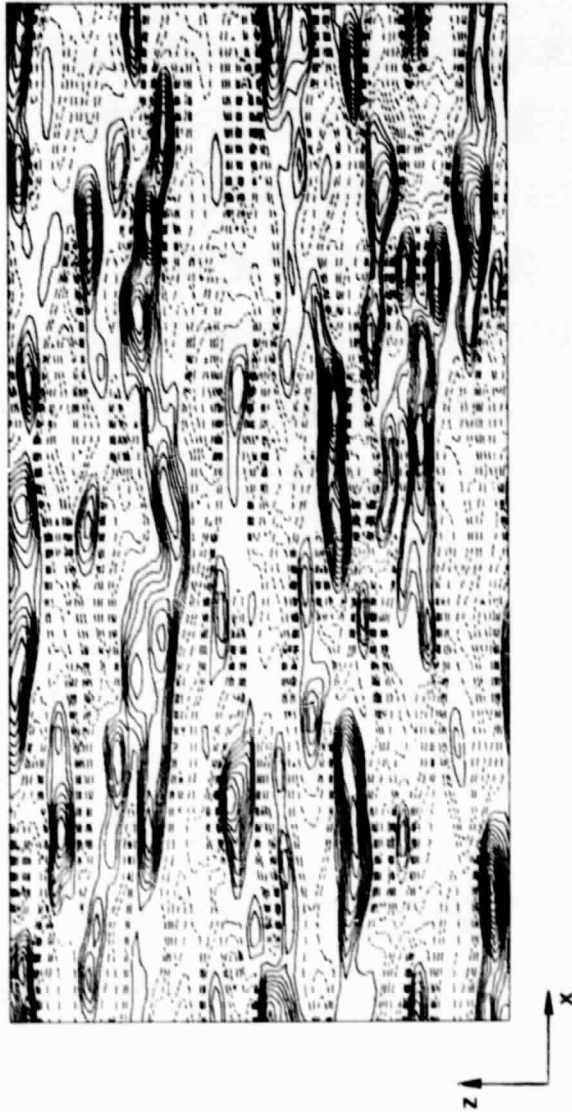
Fig. 19. Contours of $\overline{u}'$ in the x–z plane at $y^+ = 6.26$. The rectangle on the lower right-hand corner of the figure represents the computational grid cell in the x–z planes.
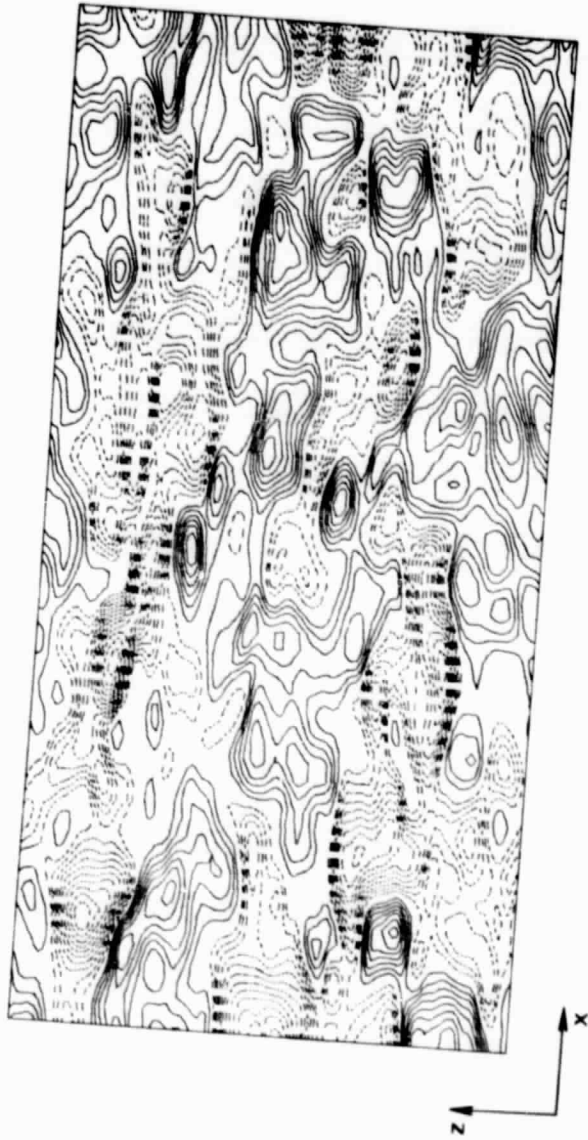
Fig. 20. Contours of $\bar{u}''$ in the x-z plane at y = -0.374.
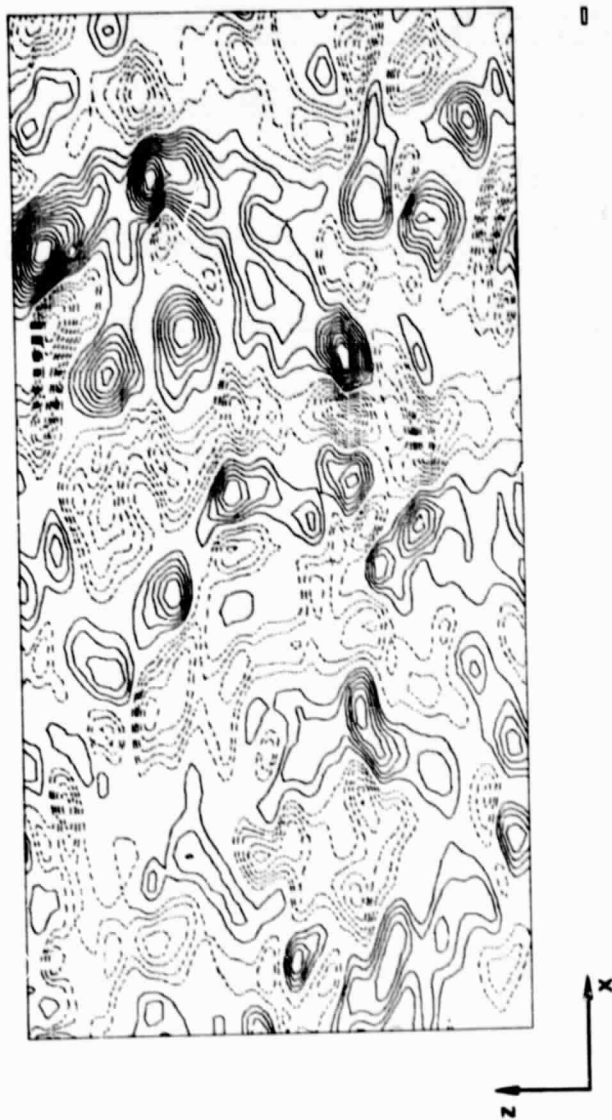
Fig. 21. Contours of P in the x-z plane at $y^+ = 6.26$.
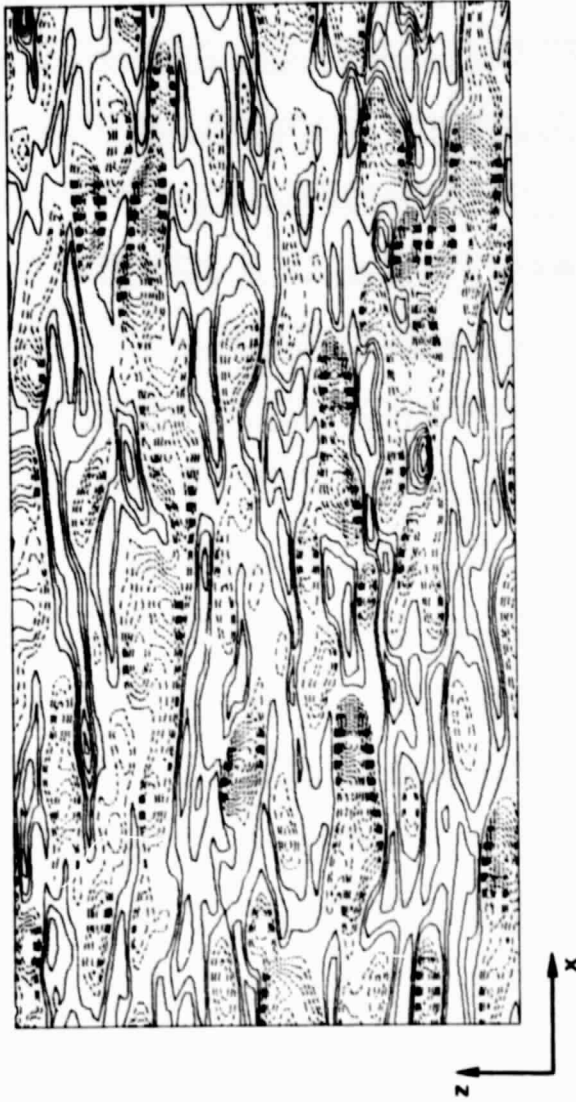
Fig. 22. Contours of spanwise vorticity fluction, ω_z'', in the x–z plane at $y^+ = 6.26$.

Fig. 23. Contours of $\overline{u}''$ in the x-y plane at $z = 4h_3$.
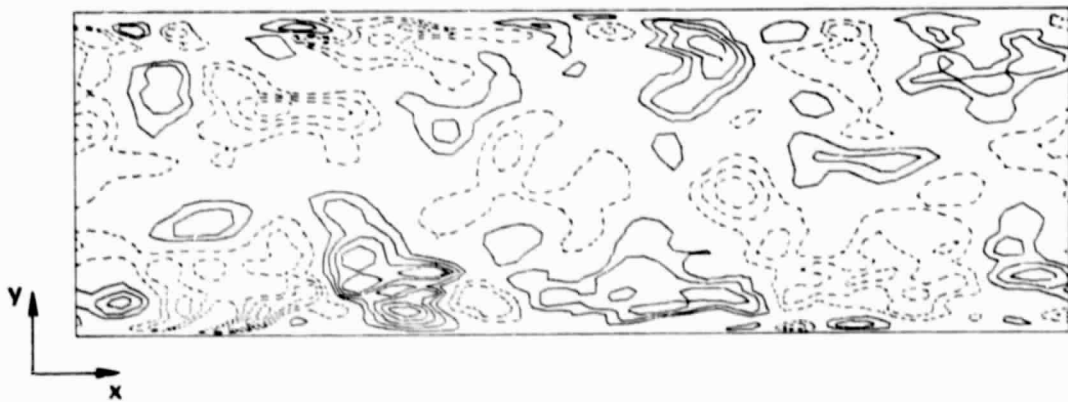
Fig. 24. Contours of $\overline{v}$ in the x-y plane at $z = 4h_3$.

63

$y_w/\delta = 1.0$

Fig. 25. Contours of $\overline{u}''$ in the y-z plane at x = 0. (Only the lower half of the channel is shown.)

$y_w/\delta = 1.0$
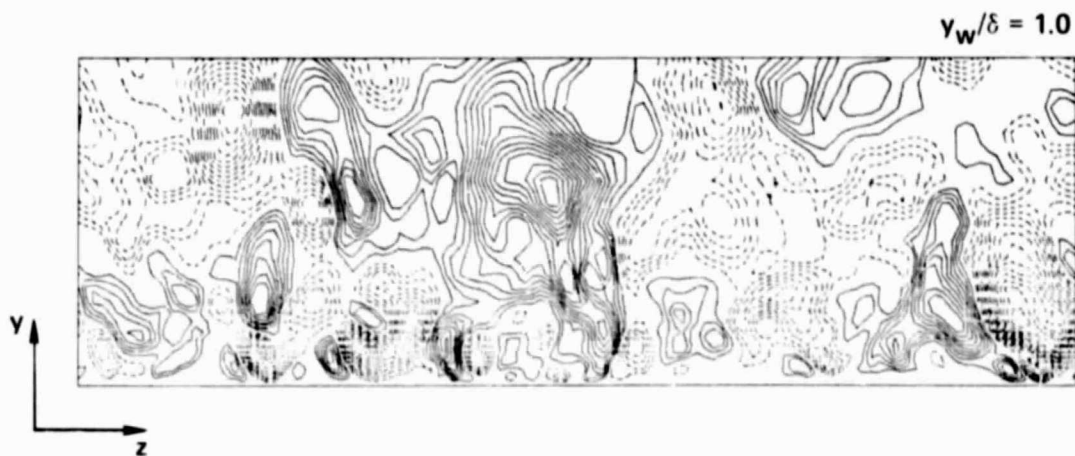
Fig. 26. Contours of $\overline{v}$ in the y-z plane at x = 0. (Only the lower half of the channel is shown.)
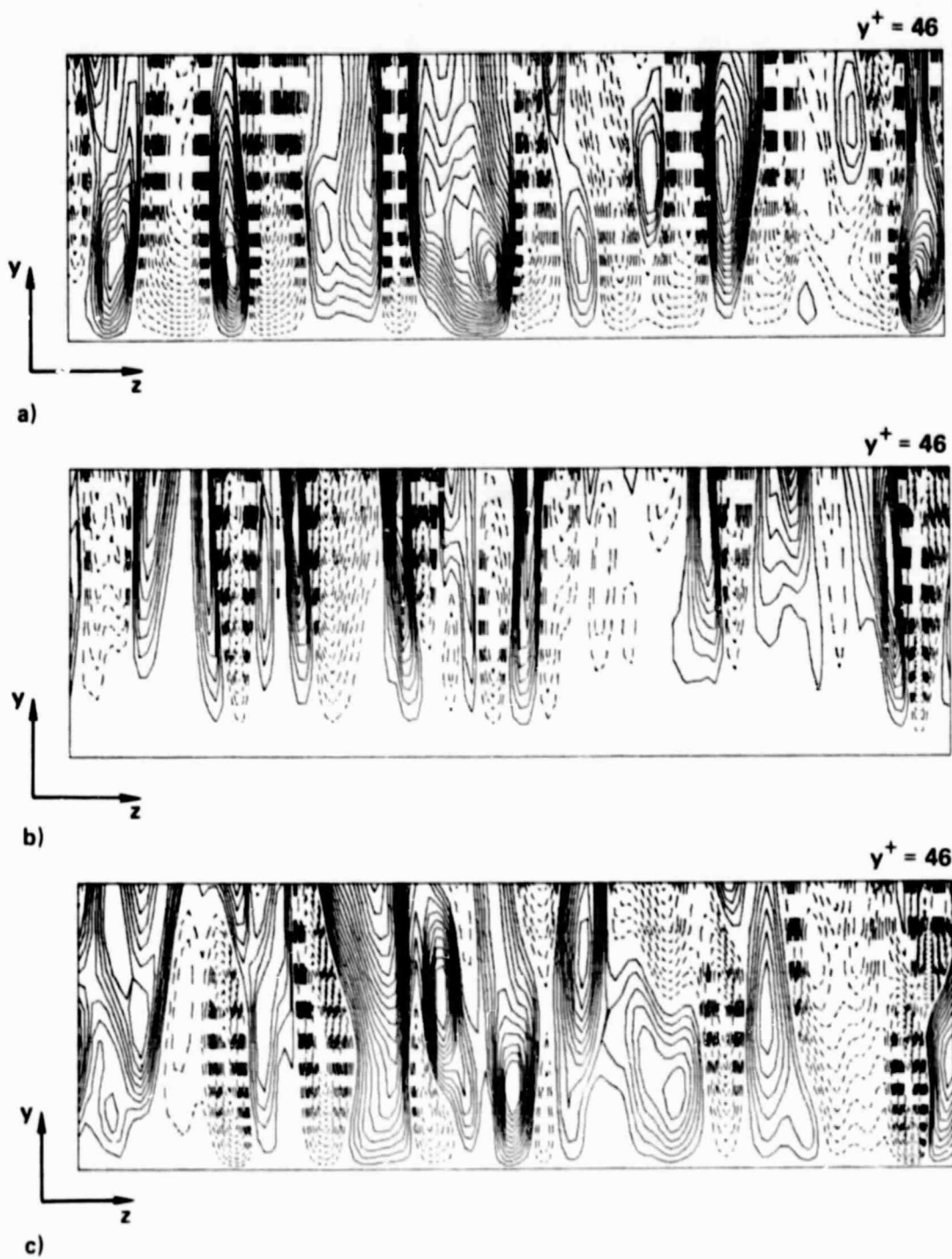
Fig. 27. Contours of $\overline{u}$ (a), $\overline{v}$ (b), and $\overline{w}$ (c) in the y-z plane ($y^+ <$ 46, $y_w/\delta < 0.072$) at $x = 0$.

$y/\delta = -0.5$

(a)

$y^+ = 46$

(b)
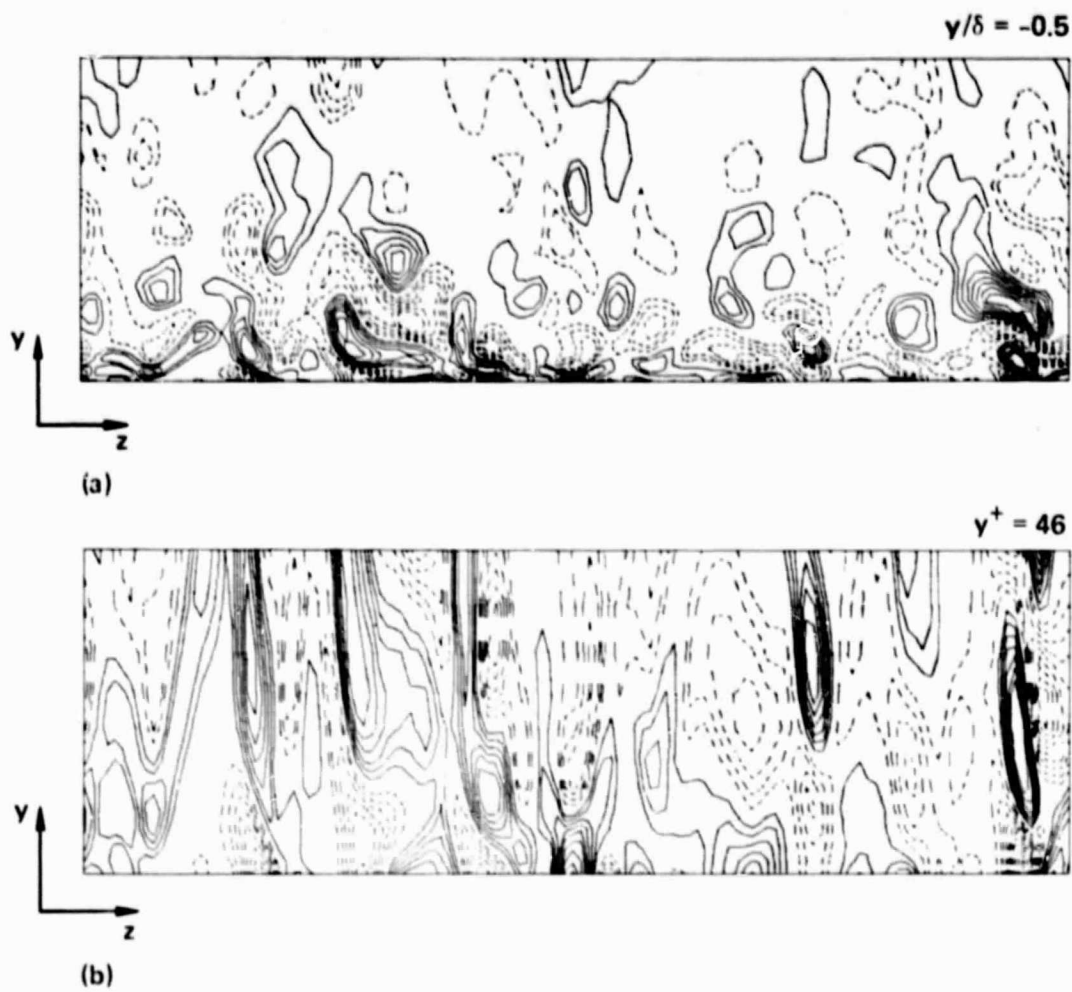
Fig. 28. Contours of streamwise vorticity fluctuations in the y-z plane at x ~ 0; (a) y < -0.5; (b) y^+ < 46.
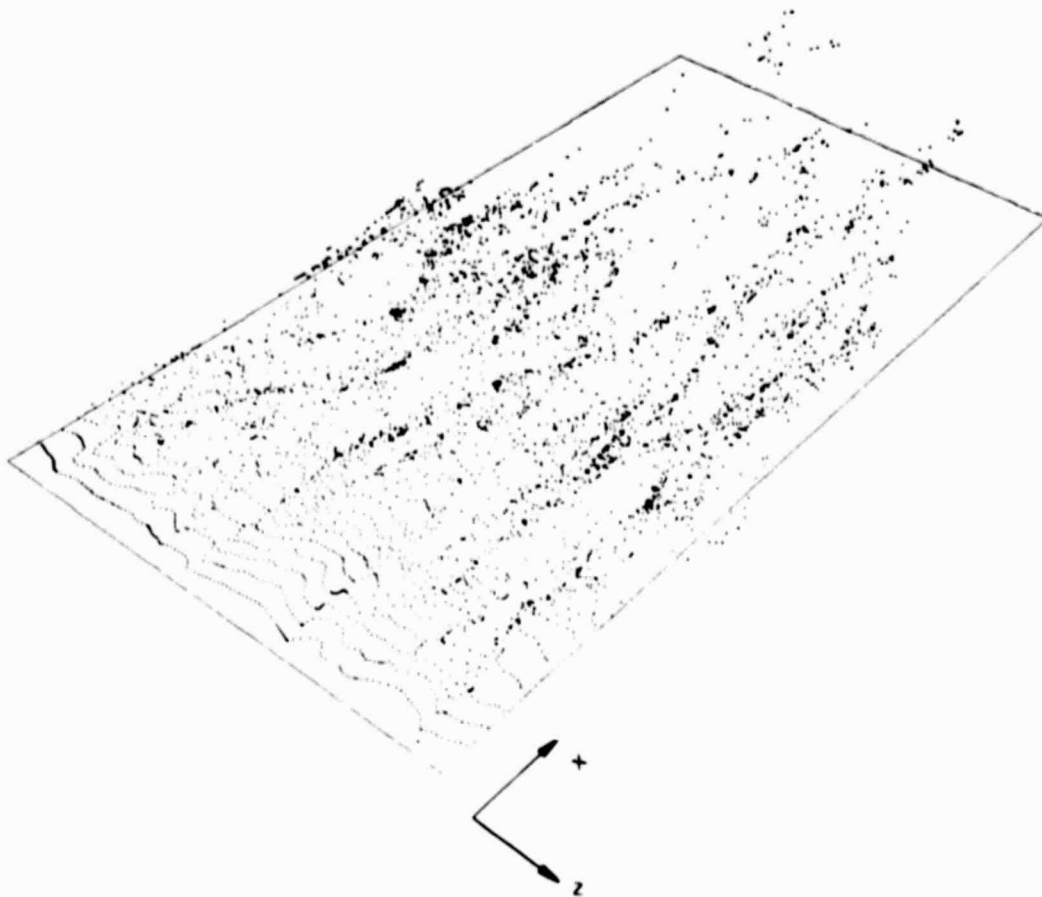
Fig. 29. Particles generated from a "z-wire" located at $y^+ = 12$.
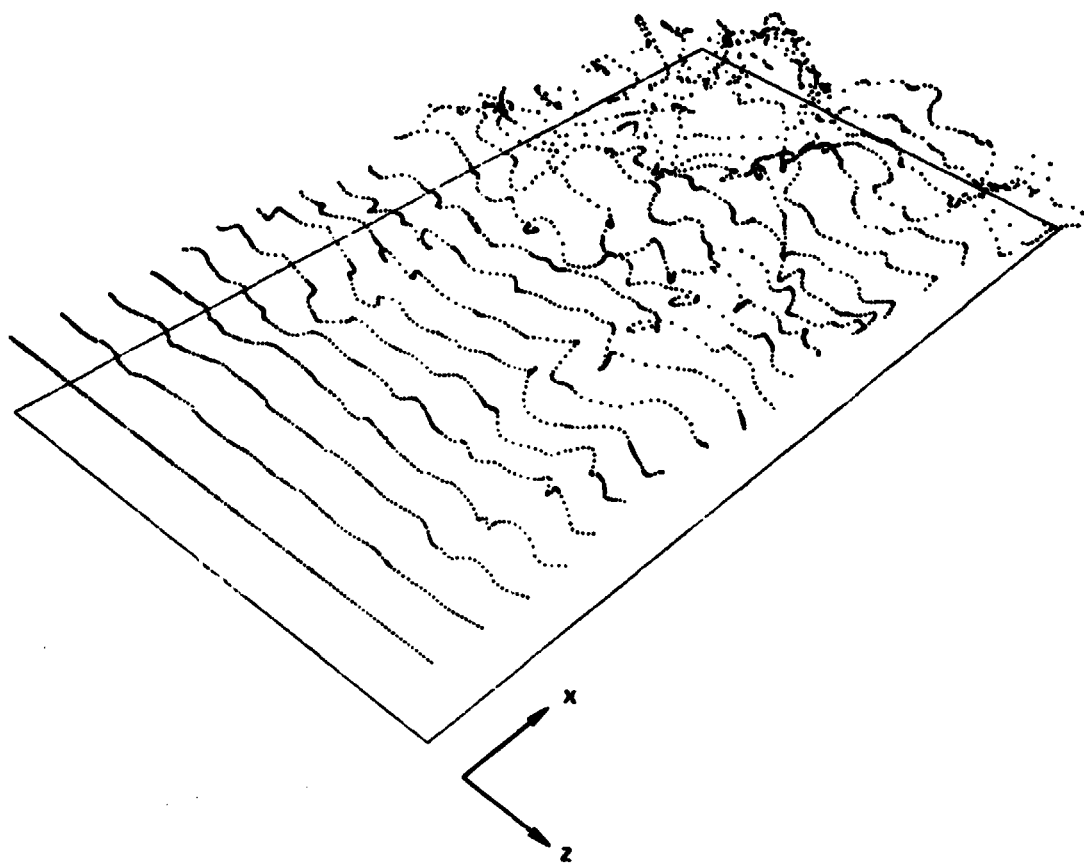
Fig. 30. Particles generated from a "z-wire" located at $y = -0.5$.

(a)

(b)
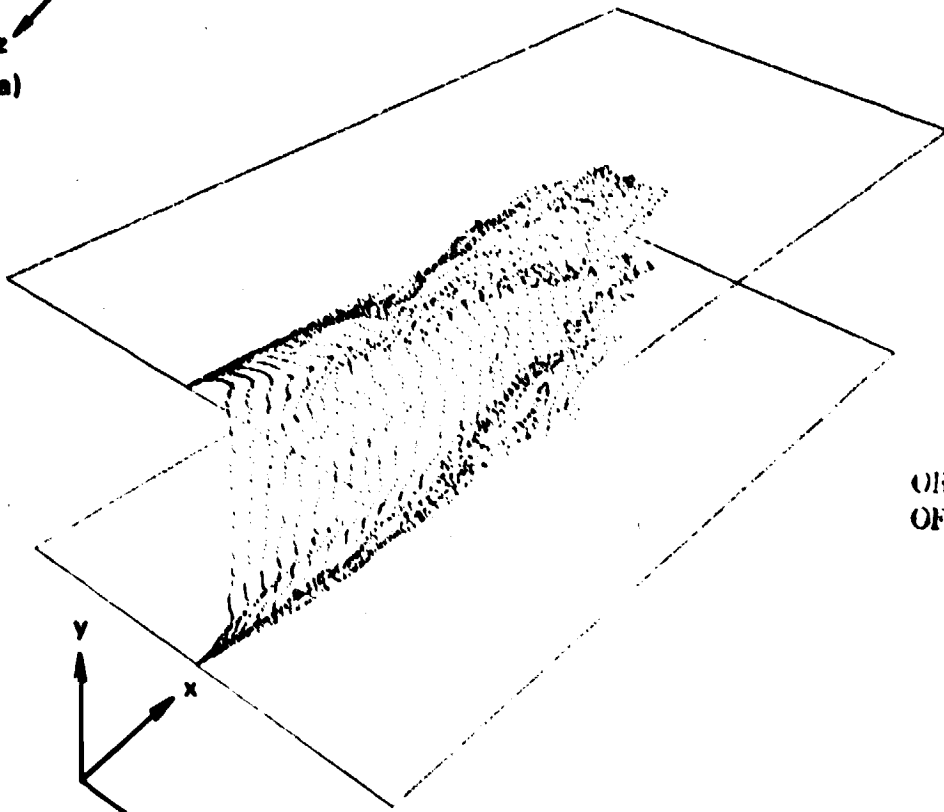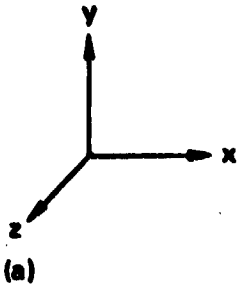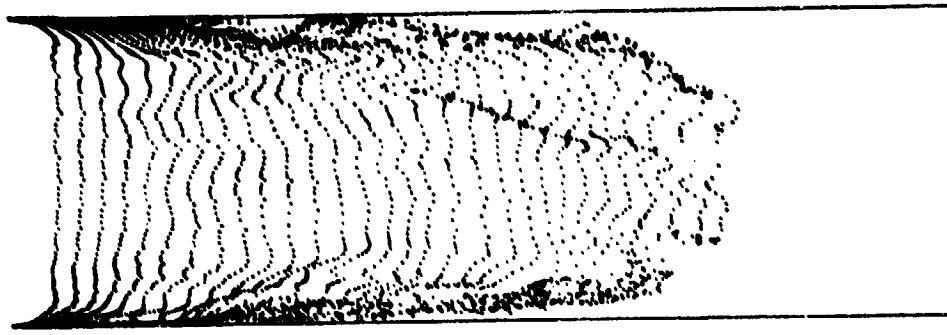
Fig. 31. Particles generated from a vertical wire extended between the two channel walls; (a) two-dimensional view; (b) three-dimensional view.
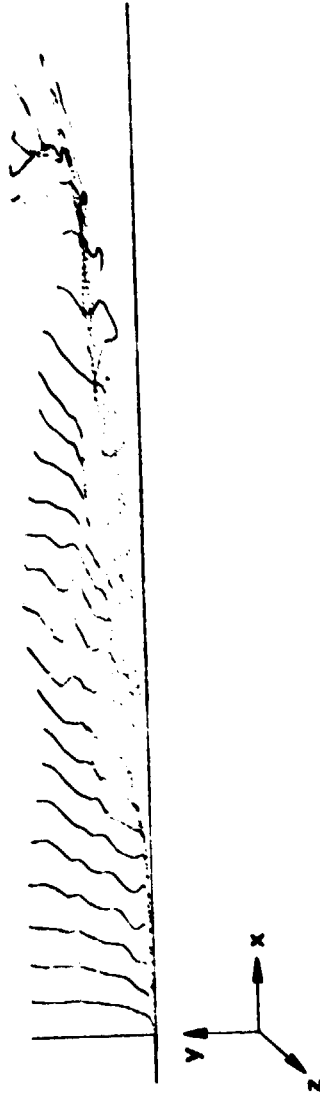
Fig. 32. Particles generated from a vertical wire extended from the lower wall to y = -0.5.